Reconstruction Methods for Optical Molecular Tomography

Alexander X. Cong

Dissertation submitted to the faculty of the Virginia Polytechnic Institute and State University in partial fulfillment of the requirements for the degree of Doctor of Philosophy in Computer Engineering

Ge Wang
Christopher G. Rylander
Peter Santago II
Chris L. Wyatt
Yong Xu

August 31, 2012, Blacksburg, Virginia

Keywords: Optical molecular imaging, reconstruction, photon propagation, finite element analysis

Reconstruction Methods for Optical Molecular Tomography

Alexander X. Cong

ABSTRACT

Molecular imaging plays an important role for development of systems biomedicine, which non-invasively extracts pictorial information on physiological and pathological activities at the cellular and molecular levels. Optical molecular tomography is an emerging area of molecular imaging. It locates and quantifies a 3D molecular probe distribution *in vivo* from data measured on the external surface of a small animal around the visible and infrared range. The reconstruction of diffuse light sources is the central task of optical molecular tomography, and generally ill-posed and rather complex. The key element of optical molecular tomography includes the geometrical model, tissue properties, photon characteristics, transport model, and reconstruction algorithm.

This dissertation focuses mainly on the **development optical molecular tomography methods based on bioluminescence/fluorescence probes** to solve some well-known challenges in this field. Our main results are as follows. **We developed a new algorithm for estimation of optical parameters based on the phase-approximation model**. Our iterative algorithm takes advantage of both the global search ability of the differential evolution algorithm and the efficiency of the conjugate gradient method. **We published the first paper on multispectral bioluminescence tomography (BLT).** The multispectral BLT approach improves the accuracy and stability of the BLT reconstruction even if data are highly noisy. **We established a well-posed inverse source model for optical molecular tomography**. Based on this model, **we proposed a differential evolution-based reconstruction algorithm to determine the source locations and strengths accurately and reliably**. Furthermore, to enhance the spatial resolution of fluorescence molecular tomography, **we proposed fluorescence micro-tomography** to image cells in a tissue scaffold based on Monte Carlo simulation on a massive parallel processing architecture. Each of these methods shows better performance in numerical simulation, phantom experiments, and mouse studies than the conventional methods.

ACKNOWLEDGEMENTS

I would like to thank my advisor, Dr. Ge Wang for all his advice, support and encouragement throughout the research of this dissertation. I would also like to thank my advisory committee members, Dr. Chris Rylander, Dr. Pete Santago, Dr. Chris Wyatt, and Dr. Yong Xu for their collaboration and guidance.

I would like to acknowledge my collaborators, Dr. Yujie Lv for providing the important mouse phantom dataset and Dr. Matthias Hoffman for his assistance with the fluorescence microtomography experiment.

I would also like to thank all the researchers, staff and students that I have had the pleasure to work with during my graduate studies, especially my fellow lab members for their valuable discussion, friendship and support.

Table of Contents

Chapter 1. Introduction 1
Section 1.1 Bioluminescence Imaging 1
Section 1.2 Fluorescence Molecular Imaging 4
Chapter 2. Photon Propagation Modeling 8
Section 2.1 Radiative Transfer Equation 9
Section 2.2 Diffusion Approximation Model 10
Section 2.3 Phase Approximation Model 12
Section 2.4 Monte Carlo Simulation 16
Chapter 3. Optical Parameter Estimation 20
Section 3.1 Mouse Modeling 20
Section 3.2 Optical Parameters 22
Section 3.3 Phase Approximation Based Identification 26
Chapter 4. Finite Element Reconstruction 37
Section 4.1 Source Reconstruction Based on Diffusion Approximation 37
Section 4.2 Multispectral Reconstruction 40
Section 4.3 Numerical Studies 42
Chapter 5. Well-posed Inverse Source Model and Reconstruction 47
Section 5.1 Well-posed Inverse Source Model 47
Section 5.2 Differential Evolution Based Solution 49
Section 5.3 Numerical Studies 54
Section 5.4 Experiments and Reconstruction Results 59
Chapter 6. Monte Carlo Fluorescence Microtomography 70
Section 6.1 Inverse Monte Carlo Reconstruction 70
Section 6.2 Experimental Studies 73
Chapter 7. Conclusion 77
Section 7.1 Main Contributions 77
Section 7.2 Software Development 78
Section 7.3 Future Topics 80
References 83
Publications 92

List of Tables

Table 3-1: Reconstructed optical parameters 34

Table 3-2: Reconstructed optical parameters for two illumination spectra 35

Table 4-1: Optical parameters of each component in the phantom 44

Table 4-2: Reconstruction results obtained using the single-band and multiband algorithms.....45

Table 5-1: Reconstruction result for two point sources.....57

Table 5-2: Reconstruction Result for Three Point Sources 57

Table 5-3: Effects of absorption coefficient variation on reconstruction results 58

Table 5-4: Effects of reduced scattering coefficient variation on reconstruction results 58

Table 5-5: Approximated optical parameters for mouse organs 65

List of Figures

Figure 2-1: The Monte Carlo process of photon propagation in tissue. 16

Figure 3-1: Mouse geometrical model. 20

Figure 3-2: Absorption spectrum of three important tissue constituents: protein (bovine serum albumin at 170 mg/g), oxyhemoglobin (40 uM) and water (40 M). The parallelogram encompasses reported values for the transport scattering coefficient of soft tissues. 24

Figure 3-3: Simulated measurements of four optical property configurations. 33

Figure 3-4: The measurements (left: GFP, right: DsRed) mapped to the surface nodes of the mouse finite element model. 35

Figure 4-1: Spectral distributions of luciferase enzymes measured using spectrometry 41

Figure 4-2: Heterogeneous mouse chest phantom with regions represent the lungs (L), bone (B), heart (H), and muscle (M). (a) Phantom geometry; (b) Source distribution in numerical simulation; (c) Source permissible region in numerical simulation. 43

Figure 4-3: Single-band and multispectral reconstructions. (a) The source distribution reconstructed using the single-band algorithm, and (b) the counterpart reconstructed using the multispectral algorithm. 45

Figure 4-4: Source densities in the single-band and multispectral reconstructions. (a) The source density reconstructed using the single-band algorithm, and (b) the counterpart reconstructed using the multispectral algorithm. 46

Figure 5-1: General structure of evolutions algorithms. 53

Figure 5-2: Simulated boundary photon fluence rate from (a) two point sources (b) three point sources. 55

Figure 5-3: Reconstruction results of two bioluminescence sources. (a) Two extra sources were assumed. (b) Exact number of sources was used. 56

Figure 5-4: Reconstruction result of three bioluminescence sources. (a) One extra source was assumed. (b) Exact number of sources was used. 57

Figure 5-5: Reconstruction result of three bioluminescence sources using conventional regularization method. 59

Figure 5-6: Mouse-shaped phantom from Caliper Life Sciences. 60

Figure 5-7: CT scan reveals LEDs' positions in the phantom. (a) sagittal view of LED 1; (b) sagittal view of LED 2; (c) axial view of LED 1; (d) axial view of LED 2. ..61

Figure 5-8: Partial surface photon fluence rate. (a) dorsal view; (b) ventral view 62

Figure 5-9: Reconstruction results of LED sources. (a) Reconstructed location of LED1. (b) Reconstructed locations of LED2. 63

Figure 5-10: Surface photon fluence mapped to mouse geometrical model. (a) dorsal view. (b) ventral view. 63

Figure 5-11: Bioluminescence tomography system with liquid nitrogen-cooled CCD camera. 64

Figure 5-12: Four bioluminescence views. (a) anterior-posterior view (b) right lateral view (c) posterior-anterior view and (d) left lateral view. 64

Figure 5-13: Reconstruction of adrenal gland tumors. (a) Finite-element model of the abdominal section of the mouse, (b) Reconstructed adrenal gland tumors vs. histological verification (c). 65

Figure 6-1: Microbead distribution in the scaffold. 73

Figure 6-2: Schematic diagram of the microbead imaging experiment. 74

Figure 6-3: Scaffold experiment results. (a) An microbead fluorescence emission image from a 0.65 mm thick scaffold; (b) a reconstructed microbead distribution from (a); (c) the projected fluorescence emission image from (b); (d) a microbead fluorescence emission image from a 0.8 mm thick scaffold; (e) the reconstructed microbeaddistribution from (d); (f) the projected fluorescence emission image from (e); (g) a microbead fluorescence emission image from a 1.4 mm thick scaffold; (h) the reconstructed microbead distribution from (g); and (i) the projected fluorescence emission image from (h). 75

Figure 6-4: Reconstructed microbead distribution (right) from fluorescence emission image of a 0.65 mm thick scaffold (center) using conventional inverse source model; the true distribution is on left. Reconstructed microbead distribution (right) from fluorescence emission image of a 0.65 mm thick scaffold (center) using conventional inverse source model; the true distribution is on the left. 76

Chapter 1. Introduction

Molecular imaging is to non-invasively monitor physiological and pathological activities in a small-animal model at the cellular and molecular levels [1, 2], specially visualize any type of cancer processes, including angiogenesis, primary tumor growth, tumor cell motility and invasion, metastatic seeding and colonization, and the relationship between the tumor and its microenvironment [3]. With the sensitive, specific, non-ionizing radiation and cost-effectiveness for detecting molecular targets in animals and humans, the optical molecular imaging has attracted a remarkable attention [4]. Fluorescent dyes or bioluminescence and fluorescent reporter proteins are stable molecules and can be easily targeted to report specific molecular processes in vivo [5-8]. Today, fluorescent and bioluminescent imaging techniques are most widely applied in preclinical studies [5-10]. The planar fluorescence/bioluminescence imaging is primarily qualitative and cannot resolve depth and quantify features. Optical molecular tomography incorporates the principles of optical tomography with the optical molecular probes as sources of contrast, and aims at quantification and localization of the internal source distribution of in tissues using light measurements of various directions on the mouse body surface. This tomographic imaging offers a superior ability to look deeper optical molecular probes inside tissues with high contrast and resolution.

Section 1.1. Bioluminescence Imaging

Bioluminescence is generated by the conversion of chemical energy into visible light by luciferase enzymes. Light-emitting bioluminescent probes, such as firefly, Gaussia, and Renillaluciferasesn enzymes, release photons when they react with substrate, oxygen and

adenosine triphosphate (ATP). The emission wavelength for the enzyme-substrate reporter is between 460 and 630 nm, allowing deep tissue penetration. The most common bioluminescence reporter genes are firefly luciferase (FLuc) and renilla luciferase (RLuc) [5, 11]. The FLuc is one of the best studied luciferase due to its high quantum yield (>88%) producing light by catalyzing the oxidation of its small molecule substrate, beetle D-luciferin (benzothiazole) in an ATP-dependent process. This luciferase emits light at a peak of 480 nm with a broad emission spectrum extending to 600 nm. Another well-studied luciferase, RLuc is from the sea pansy, Renillareniformis. RLuc utilizes coelenterazine as a substrate and emit light with a peak at 480 nm, which does not require ATP. RLuc has a low enzymatic turnover and quantum yield (6%). RLuc induces flash kinetics within the first 10 seconds which rapidly decays with time, whereas FLuc has glow kinetics. Using biological techniques, target cells can be tagged with reporters encoding several kinds of luciferase enzymes, which generate characteristic photons in a wide spectrum covering the infrared range. Bioluminescent imaging has proven to be a valuable tool for monitoring physiological and pathological activities at cellular and molecular levels in living small animals. Bioluminescence imaging (BLI) is traditionally in a planar mode as a qualitative tool.

In comparison with other optical biomedical imaging techniques, BLI is unique in terms of its sensitivity and specificity. Since the biological tissue does not emit photons while the tissue is not excited by external light, the background noise in bioluminescent imaging is very low, which results in an excellent signal-to-noise ratio. The bioluminescent photons cover a red region of the spectrum with a deep penetration depth. Hence, a significant number of the photons can escape the attenuating environment, and

be detected using a highly sensitive charge-coupled device (CCD) camera [10, 12, 13]. In 2002, the first bioluminescence tomography (BLT) prototype was conceptualized [14], and the first BLT prototype was reported that compensates for heterogeneous scattering properties of a mouse and performs quantitative 3D reconstruction of internal sources from bioluminescent views measured on the external surface of the mouse in 2003 [15]. A finite-element method based reconstruction algorithm was proposed based on the heterogeneous diffusion approximation model to recover the light source distribution. This method established a direct linear relationship between measured surface photon density and an unknown bioluminescence source distribution, and applied a permissible source region to enhance numerical stability and efficiency [16]. Adaptive finite element method was also introduced for BLT reconstructions to reduce the data memory and improve the computational efficiency comparing with the globally uniform discretization [17].

Photon migration through the biological tissue is subject to both scattering and absorption. In the biological tissue the photon scattering dominants over photon absorption. Part of the diffused light can reach the body surface of the small animal, be separated into several spectral bands using appropriate filters, and collected by a sensitive CCD camera. In 2005, a multiple spectral BLT method was proposed to reconstruct bioluminescent source from multiple spectral measurement. The multiple spectral BLT can improve the accuracy and stability of the reconstruction with noisy data [18]. Inspired by compressive sensing techniques, a novel sparse reconstruction method is proposed based on phase approximation photon propagation model [19].

This tomographic imaging modality still faces several challenges to its accuracy and stability, especially the multiple source reconstruction problems. The generic BLT problem is ill-posed, meaning it is sensitive to noise and bears multiple solutions. Recently, a regularized BLT model that incorporates the number of sources as a constraint is proposed [20]. The regularized BLT model significantly reduced the number of variables in the optimization procedure, and more importantly, produced a unique and stable solution of BLT. The new regularized inverse model and reconstruction techniques are also suitable to fluorescence and nanoparticle tomographic imaging.

Section 1.2. Fluorescence molecular imaging

The fluorophore molecule is a relatively low-energy in its ground state, and it does not fluoresce. When an external light signal at a particular wavelength hits a fluorophore molecule, the molecule would absorb sufficient photon energy, and transits to a higher energy level. After a brief interval known as the fluorescence lifetime, the fluorophore goes back to the ground state, and the excess energy is released to emit fluorescence [21, 22]. The emitted fluorescence light is of lower energy and longer wavelength than the absorbed light. Green fluorescence protein (GFP), obtained from jellyfish Aequoreavictoria, have been widely used for in vivo imaging of cells [23, 24]. DsRed is a red fluorescent protein, and distinctively exhibits an excitation wavelength of 560 nm and an emission wavelength of 580nm [25]. The stability and high intensity of brightness of DsRed make this novel fluorescent protein a viable option for optical molecular imaging. Moreover, a far-red fluorescent protein with emission spectra at 635nm, named Katushka, is also reported recently. The red fluorescent protein is strongly preferable for the visualization within living tissues and also for combining with other fluorescent proteins

in multicolor labeling [26-28]. Indocyanine green (ICG) is another useful fluorophore with near-infrared (NIR) range emission [29, 30]. The relatively low absorption and scattering of living tissue in the near-infrared (NIR) region of the electromagnetic spectrum makes near-infrared fluorescence probes important for in vivo imaging. Targeted probes typically consist of a fluorophore conjugated to a targeting ligand, e.g., an antibody that interacts and binds to a biomacromolecular of interest, thus increasing the fluorophore concentration at the target site. Such an imaging agent can be coupled to antibodies or proteins and targeted specifically to tumor cells for cancer imaging.

Planar fluorescence imaging is a useful molecular imaging modality and has proven to be a valuable noninvasive tool for monitoring physiological and pathological activities at cellular and molecular levels[31]. However, similar to BLI, the photographic imaging is primarily qualitative and cannot resolve depth and quantify features. Quantification of signal is useful for localizing a tumor in three dimensions, and helps to determine the size, volume, and depth of the lesion. The most common fluorescence imaging devices record the spatial intensity distribution of fluorescence emission qualitatively. The fluorescence intensity distribution, as an image observed at the tissue surface, is dependent on the concentration of the fluorophores at the site, the optical properties of the tissues, and the location of the fluorophores [9, 32-34]. Initial efforts focused on localization strategies for a fluorescent emission in a homogeneous medium [35, 36]. Paithankar et al. used a Newton-Raphson algorithm along with a finite difference numerical method to solve diffusion approximation equations [37]. Eppstein et al. implemented an approximated Kalman filter-based fluorescence tomography algorithm [38, 39]. Finite element-based fluorescence tomography algorithms with

Newton type optimization schemes have been proposed by Roy et al. [40] and Jiang et al. [41]. Sevick-Muraca et al. have used a finite element-based forward model with approximate extended Kalman filter to perform fluorescence tomography in clinically relevant geometries[42]. In 2001, Ntziachristos et al. presented a normalized Born approximation to facilitates fluorescence reconstructions in turbid, tissue-like media. This normalization scheme has advantages of reduced sensitivity to theoretical inaccuracies, and high robustness in imaging even at highly optically heterogeneous backgrounds, since it is independent of source strengths, detector gains and coupling efficiency to tissue [43]. This normalization scheme was pivotal to the development of the first in vivo fluorescence observations of protease up-regulation deep in mouse brains and of tumor treatment in intact animals using appropriate fluorescent probes [9, 44]. In 2003, based on the diffusion approximation model, Lee et al. presented a fully adaptive finite element method with tetrahedral elements for fluorescence molecular tomography (FMT). The adaptive methods have been shown to improve the computational efficiency and stabilization of the solution compared with the uniform discretization [45]. In 2005, Cong et al. developed a dual mode reconstruction algorithm for FMT [46], which simplified the complex nonlinear inverse problem of FMT to a linear inverse problem for fluorescent yield and an optimization problem for lifetime. The dual mode strategy helps overcome the ill-posedness for FMT reconstruction and is important for small animal imaging.

This dissertation focuses on source reconstruction techniques to solve some challenges in the field of optical molecular tomography. Our main contributions include a novel phase approximation (PA) model to describe photon propagation in the biological tissue over the visible/near-infrared spectrum range, a new reconstruction algorithm for

estimation of optical parameters based on the phase-approximation model, a novel inverse source model for optical molecular tomography, a differential evolution-based reconstruction algorithm to determine the source locations and strengths accurately and reliably, and the first fluorescence micro-tomography technique to image cells in a tissue scaffold based on Monte Carlo simulation on a massive parallel processing architecture.

Chapter 2. Photon Propagation Modeling

Optical molecular imaging employs photon-emitting biological tracers in a small animal model to reveal molecular and cellular activities in vivo [3, 4]. The propagation of light through the biological tissue is a complex course, which experiences both absorption and scattering simultaneously. Absorption occurs when the energy associated with the photon frequency matches an energy transition state within the tissue, and hence the photon energy is absorbed by the tissue. Scattering occurs when light is incident upon the atoms of the tissue. This causes the atom's electrons to accelerate and radiate in various directions, and causes light to deviate from its original path. Light propagation model describes the interaction of photons with scattering and absorbing media and are essential for tomographic imaging using visible and near-infrared light [47, 48]. The solution of the model provides basic insight into the interaction between light and tissue. The models predict light intensity distribution, which can be subsequently compared with measured light intensities on the object boundary. Based on the predicted and measured data, image reconstruction algorithms recover either the spatial distributions of intrinsic optical tissue properties or the concentrations of light emitting molecular probes inside tissue.

The radiative transfer equation well describes the photon propagation in biological tissues [49, 50]. A number of computational schemes were developed to solve the radiative transfer equation directly, such as spherical harmonics approximation method, Monte Carlo simulation [51] and discrete ordinate methods [47, 52]. Although the Monte Carlo simulation is a proven and popular stochastic method which provides highly accurate solutions of the radiative transfer equation, the high computational cost

makes it an improper choice for dealing with typical inverse problems in the biomedical imaging field. The diffusion approximation is a most widely used as a photon propagation model because of its high computational efficiency, but it only works well in weakly absorbing and highly scattering media [33, 53, 54], and breaks down with strong absorbers, near sources, across boundaries, and in the high frequency mode [50, 55].

Section 2.1. Radiative Transfer Equation

The radiative transfer equation (RTE) well describes the photon propagation in biological tissues [49, 50, 54, 56]. The steady state RTE with an isotropic source is given as:

$$\upsilon \cdot \nabla L(\mathbf{r}, \boldsymbol{\upsilon}) + (\mu_a + \mu_s) L(\mathbf{r}, \boldsymbol{\upsilon}) = \mu_s \oiint_{S^2} p(\boldsymbol{\upsilon}', \boldsymbol{\upsilon}) L(\mathbf{r}, \boldsymbol{\upsilon}') d\boldsymbol{\upsilon}' + \frac{1}{4\pi} S(\mathbf{r}), \quad \mathbf{r} \in \Omega \tag{2-1}$$

where $L(\mathbf{r}, \boldsymbol{\upsilon})$ is the photon radiance at location $\mathbf{r}$ in the direction of unit vector $\boldsymbol{\upsilon}$, $S(\mathbf{r})$ is the isotropic source, μ_s is the scattering coefficient, and μ_a is the absorption coefficient. The scattering phase function $p(\boldsymbol{\upsilon}, \boldsymbol{\upsilon}')$ gives the probability of a photon coming in the direction $\boldsymbol{\upsilon}'$ being scattered into the direction $\boldsymbol{\upsilon}$, and has the property

$$\oiint_{S^2} p(\boldsymbol{\upsilon}', \boldsymbol{\upsilon}) d\boldsymbol{\upsilon}' = 1. \tag{2-2}$$

According to optical molecular imaging experimental conditions, the boundary conditions at $\partial\Omega$ for the RTE specify that no photons travel in an inward direction at the boundary,

$$L(\mathbf{r}, \upsilon) = 0, \quad \upsilon \cdot n < 0, \quad \mathbf{r} \in \partial\Omega \tag{2-3}$$

where n is the outward unit normal at $\partial\Omega$. The RTE is an integrodifferential equation consisting of up to five independent variables (three in space and two in direction). Analytical solutions for the RTE are available for only a few simple geometries. The

RTE is often solved by numerical methods. The discrete ordinates method employs a discrete representation of the directional variation with integrals over total solid angle 4π obtained via numerical quadrature. Equation (2-1) can then be replaced by a series of equations, each describing the radiance in a specific direction. The resultant system of algebraic equations has to be solved iteratively in the presence of scattering media. The convergence of the iteration method is known to slow down for optically thick media. The spherical harmonics method converts the integro-differential RTE into relatively simple partial differential equations, which can be solved by using standard partial differential equation solver. Monte Carlo method can solve the most complicated problems by simulating radiative processes such as emission, absorption, and scattering, but this method is always subject to statistical error and requires great computational cost.

Section 2.2. Diffusion Approximation Model

The diffusion approximation (DA) is the most widely used as a photon propagation model because of its high computational efficiency and adequate accuracy in highly scattering and low absorption media [9, 10, 50, 53, 57].

Expanding the photon radiance $L(\mathbf{r},\boldsymbol{\upsilon})$ in Eq. (2-1) using spherical harmonics expansion on basis Y_l^m [50, 54].

$$L(\mathbf{r},\boldsymbol{\upsilon}) = \sum_{l=0}^{\infty} \sum_{m=-l}^{l} L_l^m(\mathbf{r}) Y_l^m(\boldsymbol{\upsilon}) \tag{2-4}$$

Taking the first order approximation in Eq. (2-4), a diffusion approximation to RTE is obtained as following:

$$L(\mathbf{r},\boldsymbol{\upsilon}) \approx \frac{1}{4\pi}\Phi(\mathbf{r}) + \frac{3}{4\pi}\boldsymbol{\upsilon}\cdot\mathbf{J}(\mathbf{r}) \tag{2-5}$$

where $\Phi(\mathbf{r})$ is the photon fluence rate, and is given as

$$\Phi(\mathbf{r}) = \oiint_{S^2} L(\mathbf{r}, \upsilon) d\upsilon \tag{2-6}$$

and $\mathbf{J}(\mathbf{r})$ is the photon flux vector, which is defined as

$$\mathbf{J}(\mathbf{r}) = \oiint_{S^2} \upsilon L(\mathbf{r}, \upsilon) d\upsilon \tag{2-7}$$

Inserting Eq. (2-5) into Eq. (2-1), RTE is converted to a coupled equation

$$\mu_a \Phi(\mathbf{r}) + \nabla \mathbf{J}(\mathbf{r}) = S(\mathbf{r}) \tag{2-8}$$

$$J(r) = -D \nabla \Phi(\mathbf{r}) \tag{2-9}$$

where $D = 1/[3(\mu_a + \mu_s')]$ is the diffusion coefficient, $\mu_s' = (1-g)\mu_s$ is the reduced scattering coefficient, and g is the anisotropic scattering factor. Plugging Eq. (2-9) into (2-8), we obtain diffusion approximation equation:

$$-\nabla \cdot [D(\mathbf{r}) \nabla \Phi(\mathbf{r})] + \mu_a(\mathbf{r}) \Phi(\mathbf{r}) = S(\mathbf{r}), \quad \mathbf{r} \in \Omega \tag{2-10}$$

Similarly derivations, the frequency domain diffusion approximation equation has following form [22, 58]:

$$-\nabla D \nabla \Phi(\mathbf{r}, \omega) + \left(\mu_a + \frac{i\omega}{c} \right) \Phi(\mathbf{r}, \omega) = S(\mathbf{r}, \omega), \quad \mathbf{r} \in \Omega \tag{2-11}$$

where ω is the modulation frequency. Based on boundary condition (2-3) of RTE, boundary condition of diffusion approximation equation can be derived by an approximation that the total in ward directed current is zero, that is

$$\int_{\upsilon \cdot n < 0} L(\mathbf{r}, \upsilon) \upsilon \cdot n d\upsilon = 0, \quad \mathbf{r} \in \partial\Omega \tag{2-12}$$

Considering the boundary refractive index mismatch between tissue and air, a fraction of the escaping photon will be reflected into domain Ω. Taking the internal boundary reflection into account, Eq. (2-12) can be modified to

$$\int_{\mathbf{v}\cdot n<0} L(\mathbf{r},\mathbf{v})\mathbf{v}\cdot n d\mathbf{v} = \int_{\mathbf{v}\cdot n>0} R\,L(\mathbf{r},\mathbf{v})\mathbf{v}\cdot n d\mathbf{v}, \quad \mathbf{r}\in\partial\Omega \tag{2-13}$$

where R is an empirically obtained parameter describing the internal reflection, and is given as $R=-1.4399\eta^{-2}+0.7099\eta^{-1}+0.6681+0.063\eta$, where $\eta = n_{tissue}/n_{air}$ [47, 53]. By evaluating the integrals, Eq. (2-13) can be further transformed into

$$\Phi(\mathbf{r})+2Dq\frac{\partial\Phi(\mathbf{r})}{\partial n}=0, \quad \mathbf{r}\in\partial\Omega \tag{2-14}$$

where $q=(1+R)/(1-R)$. In case of a source on the boundary, the boundary condition is given by

$$\Phi(\mathbf{r})+2Dq\frac{\partial\Phi(\mathbf{r})}{\partial n}+S(\mathbf{r})=0, \quad \mathbf{r}\in\partial\Omega \tag{2-15}$$

Boundary conditions Eq. (2-14) and (2-15) are known as Robin type boundary condition.

Section 2.3. Phase Approximation Model

The radiative transfer equation (Eq. 2.1) is the most accurate for modeling photon propagation in turbid media and has been adopted for tissue optics. In RTE, the scattering phase functions describe the scattering characteristics of the medium and significantly influence the precision of the solution and the efficiency of the computation. As the exact form of the phase function is currently unknown, the popular Henyey-Greenstein (HG) [59] and Delta-Eddington functions are usually used to approximate the true scattering phase functions in biomedical applications [60]. HG function was proven to be the most

accurate in terms of the angular dependence of single scattering events in the biological tissues. However, the RTE with the HG phase function is difficult to be simplified further, and need high computational costs.

An important observation is that the biological tissue scatters photons strongly in the forward direction [48, 61]. The generalized Delta-Eddington function to approximate the scattering phase function [62] is defined to describe the photon propagation,

$$p(\boldsymbol{\upsilon}, \boldsymbol{\upsilon}') = \frac{1}{4\pi}(1 - f) + \frac{1}{2\pi} f \ \delta(1 - \boldsymbol{\upsilon} \cdot \boldsymbol{\upsilon}') \tag{2-16}$$

where $f \in [-1, +1]$ is a free weighting factor measuring the anisotropy of photon scattering, which we call the anisotropy weight [62, 63]. The phase function is a linear combination of the isotropic scattering and the strongly peaked forward scattering with the anisotropy weight f as a coefficient depending on the tissue type. In contrast to the original Delta-Eddington phase function in which the parameter f takes a fixed value g being the mean of the cosine of the scattering angles, our generalized Delta-Eddington phase function defines f as a variable, which is related to the photon absorbing and scattering coefficients in the biological tissue. The scattering phase function is a linear combination between the isotropic scattering and the strongly peaked forward scattering. The new characteristics of the generalized Delta-Eddington function are that the anisotropy weight can be adjusted according to photon absorption and scattering properties to obtain an accurate approximation to the true scattering function. With the new definition of our generalized phase function, the radiative transfer equation can be significantly simplified into an integral equation in terms of photon fluence rate. For

simplicity, we call it the phase approximation (PA) model because it is derived from an approximate phase function.

Substituting Eq. (2-16) to Eq. (2-1) yields:

$$\boldsymbol{\upsilon}\cdot\nabla L(\mathbf{r},\boldsymbol{\upsilon})+\hat{\mu}_t L(\mathbf{r},\boldsymbol{\upsilon})=\frac{1}{4\pi}\left(\hat{\mu}_s\Phi(\mathbf{r})+S(\mathbf{r})\right),\quad \mathbf{r}\in\Omega \tag{2-17}$$

where $\hat{\mu}_s=(1-f)\mu_s$, $\hat{\mu}_t=\mu_a+\hat{\mu}_s$, and the photon fluence rate $\Phi(\mathbf{r})$ is defined in Eq. (2-6). Equation (2-17) is a first-order differential equation, and has a closed form solution:

$$\begin{aligned}L(\mathbf{r},\boldsymbol{\upsilon})=&\frac{1}{4\pi}\int_0^R\left[\hat{\mu}_s(\mathbf{r}-\rho\boldsymbol{\upsilon})\Phi(\mathbf{r}-\rho\boldsymbol{\upsilon})+S(\mathbf{r}-\rho\boldsymbol{\upsilon})\right]\exp\left(-\int_0^\rho\hat{\mu}_t(\mathbf{r}-t\boldsymbol{\upsilon})dt\right)d\rho\\&+L(\mathbf{r}-R\boldsymbol{\upsilon},\boldsymbol{\upsilon})\exp\left(-\int_0^R\hat{\mu}_t(\mathbf{r}-t\boldsymbol{\upsilon})dt\right)\end{aligned} \tag{2-18}$$

where $\mathbf{r}-R\boldsymbol{\upsilon}\in\partial\Omega$, R represents the distance from position $\boldsymbol{r}$ to the boundary $\partial\Omega$. Integrating Eq. (2-18) over all the solid angles, we get the following integral formula:

$$\begin{aligned}\Phi(\mathbf{r})=&\frac{1}{4\pi}\oiint_{S^2}\int_0^R\left[\hat{\mu}_s(\mathbf{r}-\rho\boldsymbol{\upsilon})\Phi(\mathbf{r}-\rho\boldsymbol{\upsilon})+S(\mathbf{r}-\rho\boldsymbol{\upsilon})\right]\exp\left(-\int_0^\rho\hat{\mu}_t(\mathbf{r}-t\boldsymbol{\upsilon})dt\right)d\rho d\boldsymbol{\upsilon}\\&+\oiint_{S^2}L(\mathbf{r}-R\boldsymbol{\upsilon},\boldsymbol{\upsilon})\exp\left(-\int_0^R\hat{\mu}_t(\mathbf{r}-t\boldsymbol{\upsilon})dt\right)d\boldsymbol{\upsilon}\end{aligned} \tag{2-19}$$

The reflected radiance $L(\mathbf{r}-R\boldsymbol{\upsilon},\boldsymbol{\upsilon})$ describes the contribution from the reflected photons on the boundary caused by the refractive index mismatch between biological tissues (n_{tissue}) and air (n_{air}), and can be approximated by

$$L(\mathbf{r}-R\boldsymbol{\upsilon},\boldsymbol{\upsilon})=\approx\frac{r_d}{4\pi(1+r_d)}\Phi(\mathbf{r}) \tag{2-20}$$

where the internal reflection coefficient r_d can be calculated from $r_d = -1.4399\eta^{-2} + 0.7099\eta^{-1} + 0.6681 + 0.063\eta$, and $\eta = n_{tissue}/n_{air}$. Finally, an integral equation with respect to photon fluence rate $\Phi(\mathbf{r})$ is obtained by performing a variable transformation from the polar coordinate to Cartesian coordinate:

$$\Phi(\mathbf{r}) = \frac{1}{4\pi}\iint_{\Omega} G(\mathbf{r},\mathbf{r}')[\hat{\mu}_s(\mathbf{r})\Phi(\mathbf{r}) + S(\mathbf{r})]d\mathbf{r}' - \frac{r_d}{4\pi(1+r_d)}\oint_{\partial\Omega} G(\mathbf{r},\mathbf{r}')\Phi(\mathbf{r})\boldsymbol{\beta}\cdot n d\mathbf{r}' \qquad (2\text{-}21)$$

where

$$G(\mathbf{r},\mathbf{r}') = \frac{1}{|\mathbf{r}-\mathbf{r}'|^2}\exp\left(-\int_0^{|\mathbf{r}-\mathbf{r}'|}\hat{\mu}_t(\mathbf{r}-t\boldsymbol{\beta})dt\right) \qquad (2\text{-}22)$$

Unit vector $\boldsymbol{\beta} = (\mathbf{r}-\mathbf{r}')/|\mathbf{r}-\mathbf{r}'|$, and n is the outward unit normal on the boundary surface at $\mathbf{r} - R\boldsymbol{\beta}$. Eq. (2-21) is the second kind of integral equation and allows accurate modeling of photon propagation in biological tissues. In contrast to the diffusion approximation model derived from the first order approximation of the photon radiance, the phase approximation model is based on the exact computation of the photon radiance in the biological tissue [62]. The phase approximation methodology removes the limitation of scattering dominating photon propagation in the diffusion approximation model. The new model is highly accurate over a broad range of optical coefficients as well as near sources and boundaries. While the RTE is a five dimensional computational problem (three dimensional space and two dimensional direction vector), the phase approximation model is three dimensional computational problem which is same to that of the diffusion approximation model.

Section 2.4. Monte Carlo Simulation

Monte Carlo simulation is a statistics method to solve complex problems by simulating the statistical behavior of a large number of individual entities and analyzing their collective features. For example, it can be used to compute highly complex integrals over irregular domains, such as in the semiconductor industry. The Monte Carlo simulation technique has been extensively studied in the field of high energy physics to investigate particle transfer. EGS5 and Geant4 are exemplary software simulation packages developed for this purpose and have been used in numerous studies. Typically, the photon scattering in turbid media is very complex. In some photon transport processes, the number of scattering events for each photon is limited, such as in the case of x-ray and tissue interaction. For other transport processes, the photon will move in a pronounced zigzag pattern. For example, biological tissues generally have a relatively high scattering coefficient for visible light, and the behavior of the photon can be described by the average scattering angle without the detailed scattering profile. Based on key optical parameters including the absorption coefficient, scattering coefficient and anisotropy factor, efficient optical Monte Carlo simulation is feasible for use in biological tissues.

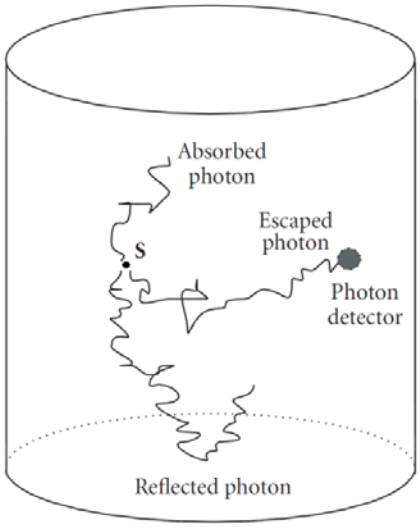

Figure 2-1. *The Monte Carlo process of photon propagation in tissue*

Monte Carlo (MC) simulation models each individual photon's physical interactions with the medium as a stochastic process. As a large number of such stochastic processes of photon

propagation are simulated, the signal detected is statistically meaningful and very close to the physical experiment counterpart. MC result can be legitimately considered as the low-noise version of the actual physical measurement. The Monte Carlo process consists of three parts: the photon absorption, the photon scattering and the internal reflection at the boundaries, as illustrated in Figure 2-1.

The Monte Carlo method relies on the random sampling of variables from probability distribution[51]. For random variable χ, there is a probability density function $p(\chi)$ that defines the distribution of χ over the interval (a, b). This variable may be the angle of deflection that a scattered photon may experience due to a scattering event, or the variable step size that a photon will take between photon-tissue interaction sites. To simulate propagation, we need to choose a value for χ randomly based on a pseudo-random number generator. The value is a random variable ξ, which is uniformly distributed over the interval (0, 1). The generally non-uniform probability density function $p(\chi)$ is sampled by solving the following equation for χ,

$$\int_a^{\chi} p(x)dx = \xi \quad \text{for} \quad \xi \in (0,1) \tag{2-27}$$

A photon is uniquely described by five variables: three spatial coordinates for the position and two directional angles for the direction of travel. However it is convenient to describe the photon's spatial position with three Cartesian coordinates and the direction of travel with three direction cosines. The angle variables describing photon direction do not change unless the photon's direction changes. The direction cosines are specified by taking the cosine of the angle that the photon's direction makes with each axis. The

possibility of internal reflection occurs when the photon is propagated across a boundary into a region with a different index of refraction. The probability that the photon will be internally reflected is determined by the Fresnel reflection coefficient. The internal reflectance rate due to the refractive index mismatch at the tissue boundary for unpolarized incident light is given by the Fresnel's formulas [2, 3]:

$$R(\alpha_i) = \frac{1}{2}\left[\frac{\sin^2(\alpha_i - \alpha_t)}{\sin^2(\alpha_i + \alpha_t)} + \frac{\tan^2(\alpha_i - \alpha_t)}{\tan^2(\alpha_i + \alpha_t)}\right] \tag{2-28}$$

where α_i and α_t are the incident and transmit angles, respectively. The incident and transmit angles obey the Snell's law

$$\frac{\sin\alpha_i}{\sin\alpha_t} = \frac{n_t}{n_i} \tag{2-29}$$

where n_i and n_t are the refractive indices for both sides of the boundary, respectively. After each propagation step, the photon packet is split into two parts, a fraction is absorbed and the rest is scattered. The absorption of photon for each step can be express by

$$\Delta W = \frac{\mu_a}{\mu_a + \mu_s} W \tag{2-30}$$

where W is the weight of the photon packet. Once the photon packet has reached an interaction site and its weight decreased, the photon packet with the updated weight is ready to be scattered. If the phase function has no azimuthal dependence, then the azimuthal angle ϕ is uniformly distributed between 0 and 2π, and may be generated by multiplying a pseudo-random number ξ uniformly distributed over the interval zero to one by 2π, $\phi = 2\pi\xi$. Scattering in tissue is characterized by the Henyey-Greenstein phase function, which produces

$$\cos\theta = \frac{1}{2g}\left[1 + g^2 - \left(\frac{1-g^2}{1-g+2g\xi}\right)^2\right] \tag{2-31}$$

where θ is the deflection angle, and g the anisotropy parameter. If a photon is scattered at an angle (θ,ϕ) from the direction (v_x, v_y, v_z) in which it is travelling, then the new direction (v'_x, v'_y, v'_z) is specified by

$$\begin{cases} v_x = \dfrac{\sin\theta}{\sqrt{1-v_z^2}}\left(v_x v_z \cos\phi - v_y \sin\phi\right) + v_x \cos\theta \\ v_y = \dfrac{\sin\theta}{\sqrt{1-v_z^2}}\left(v_y v_z \cos\phi + v_x \sin\phi\right) + v_y \cos\theta \\ v_z = -\sin\theta\cos\phi\sqrt{1-v_z^2} + v_z \cos\theta \end{cases} \tag{2-32}$$

After a photon packet is launched, it can be terminated naturally by reflection or transmission out of the tissues. We programmed MCsim [14], a Monte Carlo simulator, for the photon propagation for the numerical experiment. Our MC simulator can handle several types of 3D geometrical phantoms such as cylinders and ellipsoids. By combining cylinders and ellipsoids, which can represent different mouse organs, the heterogeneous phantom mimicking the real mouse is created. The MC simulation based on such heterogeneous numerical phantom is similar to the in vivo mouse experiment. The efficiency of the MC simulation is enhanced through the parallel computing and fast random array generation.

Chapter 3. Optical Parameter Estimation

Optical molecular tomographic imaging is to reconstruct the density distribution of photon-emitting sources inside tissue from boundary measurements. The reconstruction of light sources is related to the mouse geometrical model, tissue optical properties, photon spectrum characteristics, and photon propagation model. The anatomical information of a small animal can be obtained from structural imaging techniques (i.e. x-ray CT, MRI) and tissue optical properties can be reconstructed using optical tomography. These can be used as prior information for the reconstruction of light source distribution.

Section 3.1. Mouse modeling

Mouse body is soft tissues, and mouse anatomical shape would vary with a different posture. We need to design an imaging system with a special mouse holder to keep the mouse in an identical posture in the entire imaging procedure. A living mouse in the holder is individually scanned using Micro-CT (or MIR) to delineate its anatomy, and be compared with a surface scan of the same mouse to confirm the consistency of the body posture. Then, these CT images are segmented into organ regions of the mouse and assembled into a geometrical model using computer graphic techniques. Because the mouse anatomy is

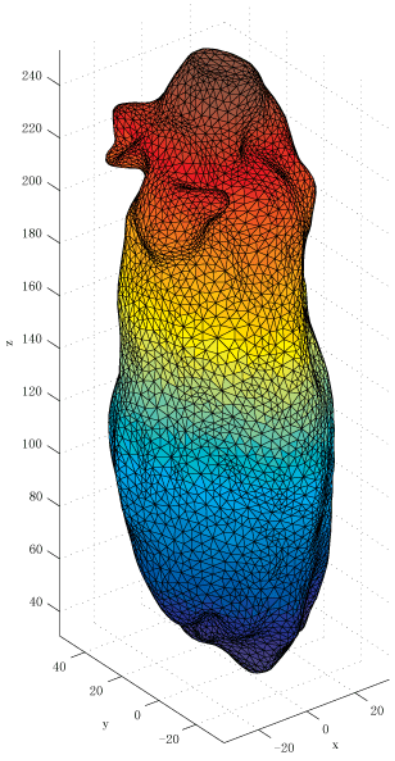

Figure 3-1. *Mouse geometrical model.*

rather complex, it is difficult to present all the features in a geometrical model. Also, the computation would become impractical with an overcomplicated geometrical model. Hence, based on this tomographic image volume and in reference to a high-resolution atlas which is built independently, we segment the image volume into major organ regions approximately at ~0.5mm resolution, such as lungs, liver, heart, kidneys, stomach, bone and muscles. In the early 1987, the Marching Cubes (MC) algorithm was proposed to extract isosurface from CT/MR image volume for generating geometrical model. The algorithm visits each cell formed by eight adjacent voxels in the image volume and performs local triangulation by interpolate new vertices along the cell edges. The isosurface extraction algorithms only extract surface of a single material for one sweep of the CT/MR image volume. We have proposed a Multiregional Marching Tetrahedra (MMT) algorithm to extract surfaces of different anatomical components from segmented CT/micro-CT images of mice within a single pass. The extracted surfaces are smoothed and simplified to serve as a proper geometrical model. Our MMT algorithm can also construct multiple material finite element meshes directly from CT image volume for finite element numerical computation [73]. Deformation technique is also used to fast construct geometrical models from a base geometrical model with similar geometrical shape. This would significantly simplify the geometric modeling task for widest practical use. At present, a commercial software, such as Amira 4.0 (Mercury Computer Systems, Inc. Chelmsford, MA), has been developed using the computer graphic techniques to generate a geometrical model of the mouse from these segmented CT images [64], as shown in Fig. 3-1. Based on the 3D geometrical model, we can generate a high-quality finite-element mesh. In this way, a set of standard finite element

geometrical models has been already established in our Biomedical imaging Division for different weights and sizes of mice.

Furthermore, a computer controlled laser galvanometer projects parallel laser lines onto a mouse body and reconstructs the mouse body surface from four directions. Then, based on the surface shape of the mouse, a finite element geometrical model of a mouse can be obtained by elastically deforming the known finite element geometrical models. Although the real mouse may differ from any standard mouse model, the differences can be minimized using an elastic registration technique, such as an affine transformation. To deform a selected mouse model in reference to the individual mouse surface, we specify corresponding points keyed to anatomical landmarks on the model and real mice. Then, the one-to-one correspondence can be optimally established between the generated finite element mouse model and a real mouse to generate the finite element geometrical model. Recently, a dual-modality system that combines optical molecular imaging and x-ray micro-CT has been developed to simultaneously reveal molecular and structural information in small animals. Clearly, the dual-modality imaging methodology can provides correct anatomical information for optical molecular tomography and create functional images with accurate localization of fluorophore distribution.

Section 3.2. Optical Parameters

Optical properties of biological tissues are typically characterized by the absorption coefficient μ_a, the scattering coefficient μ_s, and the angular scattering probability distribution (or phase function) $P(\theta)d\theta$ for scattering by an angle between $\theta + d\theta$ and θ

.

Absorption Coefficient: The linear absorption coefficient of tissue can be determined from the concentration and molecular cross section of all chemical species present. In the ultraviolet region of the spectrum tissue absorption is dominated by proteins. Not only is the concentration of proteins high, the amino acids phenylalanine, tyrosine, and tryptophan are efficient absorbers in the 250 nm to 300 nm range. As the wavelength increases, protein absorption decreases rapidly and other chromophores, especially hemoglobin, become dominant. Haemoglobin consists of the protein globin bound to four haem groups. Each haem group contains an iron atom at the centre of aring-like structure. An iron atom in the ferrous (Fe2+) form will bind physically to an oxygen molecule to become oxygenated. One haemoglobin molecule with its four iron centres can carry a total of four molecules of oxygen. In the oxygenated state haemoglobin is known as oxyhaemoglobin (HbO2). The de-oxygenatedform, with no oxygen molecules attached, is known as deoxyhaemoglobin (Hb). The individual absorption peaks of hemoglobin and the change in spectrum with oxygenation can be readily observed *in vivo.* The infrared absorption of tissue is dominated by its most abundant chromophore, water. The vibrational modes of the O-H bond produce a series of peaks with the maximum occurring at 2.95 microns. The concentration of principal tissue chromophores will vary from tissue to tissue and other pigments may be significant in organs, such as the liver and the skin. Fig. 3-2 correctly predicts the order of magnitude of tissue absorption and the main features of its dependence on wavelength.

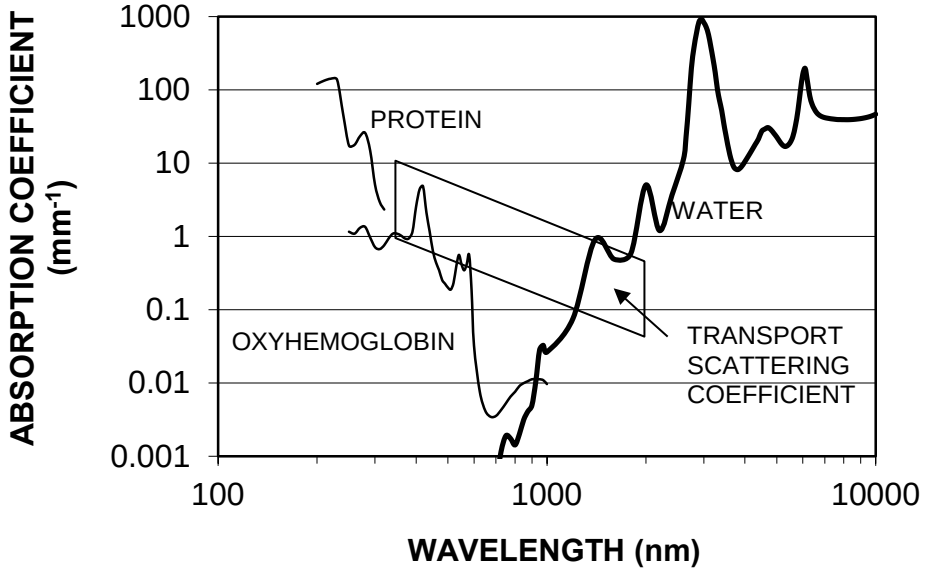

Figure 3-2. *Absorption spectrum of three important tissue constituents: protein (bovine serum albumin at 170 mg/g), oxyhemoglobin (40 μM) and water (40 M). The parallelogram encompasses reported values for the transport scattering coefficient of soft tissues [61].*

Scattering Coefficient: The scattering coefficient μ_s and the scattering cross-section σ_s are related as $\mu_s = \rho\sigma_s$, where ρ is the particle number density in the medium. Scattering of light in tissue is caused by inhomogeneities such as cell membranes or intracellular structures. The scattering arises due to a relative refractive index mismatch at the boundaries between two such media or structures, e.g. between the extracellular fluid and the cell membrane. Tissue is a complex medium in which the index of refraction varies in a complex way over different length scales in different tissues. Each microscopic scattering particle will give rise to its own scattering phase function, which depends on the physical properties of the object. A single scattering event in tissue can be considered to arise from an averaged scattering object, representing a distribution of scattering objects with an averaged phase function. The contribution of each type of object to the

averaged scattering properties in tissue depends on their individual scattering properties and their relative concentrations.

Haemoglobin molecules comprise approximately 97% of the cell solids. The erythrocyte has a biconcave shape, with a main diameter of approximately 8 μm and across-sectional thickness of 1–2 μm. The cell is bound by a membrane approximately 8 nm in thickness. Fibrous proteins in the membrane allow the cells enough flexibility to deform their shape, in order to fit through capillaries of smaller diameters than themselves. Since there is a refractive index mismatch between the cell membrane and the surrounding medium, i.e. plasma in whole blood, the red blood cell will scatter light. The refractive index of the red blood cell is about 1.4 ± 0.01 and that of blood plasma is 1.34. The scattering coefficient is very high when compared to low energy x-rays. Typical values at visible wavelengths are 10 to 50 mm^{-1}, corresponding to a mean free path of 20 to 100 microns. In general, the scattering coefficient is observed to decrease monotonically as the wavelength increases although few studies have been performed over a wide spectral range. Generally, the scattering coefficient is orders of magnitude larger than the absorption coefficient.

Scattering Phase Function: On encountering a scattering particle within a homogeneous medium, photons travelling in a direction ŝ are scattered into a new direction š. The new directions generally do not occur with equal probability and can be described by the angular scattering probability distribution $p(\hat{s},\breve{s})$. If the scattering is completely isotropic then $p(\hat{s},\breve{s})$ is equal for all angles and g will be equal to zero. As the particle size increases, however, the intensity distribution increases in the forward direction and the

scattering phase function for small angles is much higher than for all other angles. Therefore, the mean cosine g of the scattering angle tends towards a value of unity, the higher the g value the more forward-peaked the scattering. Biological tissue strongly scatters photon in the peaked forward, and typical values of the anisotropy parameter for tissue are 0.9 or higher in the visible. The Henyey–Greenstein scattering phase function is used often for light propagation in tissues [51, 59]. This model features both forward-peaked scattering and large-angle scattering. It has been shown to compare well with experimental measurements. The delta-Eddington approximation was introduced by Joseph et al. [60] as an extension to the two-term Eddington approximation to study forward-peaked and large-angle scattering. It is also a two-order approximation to Henyey–Greenstein scattering phase function [65].

Section 3.3. Phase Approximation Based Identification

Estimation of optical properties of biological tissue is an essential task for optical imaging applications. In Section 2.3 we introduced the phase approximation model (PA). Our PA model approximates the phase function in RTE using the generalized Delta-Eddington phase function instead of the commonly used Henyay-Greenstein function. The generalized Delta-Eddington phase approximation greatly simplified RTE to PA model, which has an accuracy comparable to that of the original RTE and can be solved efficiently. However, the PA model has a unique reduced scattering coefficient $\hat{\mu}_s$ that must be determined in order to be practically used in optical imaging applications. Optical property estimation that is based on the PA model will inherently yield accurate optical parameters for a wide range of tissue properties. The accuracy of the optical parameters characterization, however, does not solely depend on the accuracy of the

forward model; the iterative algorithm could converge prematurely to an inaccurate solution if the initial guess is not close enough to the true solution. Fortunately, differential evolution is an effective global search method to find a good starting point quickly. In this section, we focus on the optical property characterization of a homogeneous biological tissue under the PA model. We introduce a method for estimating the optical parameters for the PA model by matching the calculated and measured photon fluence rates iteratively. The iterative procedures based on gradient-guided optimization are sensitive to initial guesses. By combining the global search ability of the stochastic algorithm and the efficiency of the gradient-guided optimization method, we are able to obtain an accurate, efficient and robust parameter reconstruction.

The optical parameters of tissues can be determined in two ways. If the absorption coefficient, scattering coefficient and conventional anisotropic factor in the tissue are known, we can determine the anisotropy weight for the phase approximation model in an indirect way. In this case, we just need to simulate a homogenous numerical phantom, like a spherical or cylindrical object with the known absorption coefficient, scattering coefficient and anisotropic factor. Then, a single parameter optimization can be performed with respect to the anisotropy weight by matching the computed data based on the phase approximation model to the Monte Carlo simulation results. On the other hand, our preferred method is the following direct way. When the absorption coefficient, scattering coefficient and conventional anisotropic factor in the tissue are all unknown, we will use the phase-approximation-based optical tomography (POT) to estimate the in vivo optical parameters of major mouse regions defined in the corresponding geometrical model. In POT, appropriate laser beams corresponding to nanoparticle spectral range

will irradiate the mouse body and generate diffuse signals. Typically, lasers excite the mouse body at various locations so that sufficiently strong light signals transmit through every major mouse tissue types. The transmitted diffusive light signal is measured on the opposite side of the mouse body. Hence, we can obtain excitation-diffusion measurement datasets using the optical imaging system. We further assume that the optical properties are constant in the same tissue type or organ region. As a result, this POT approach only deals with a much less number of unknown optical parameters than the traditional DOT approach does [54, 66, 67], which helps improve the numerical stability of the reconstruction for optical parameters. Furthermore, the reconstruction of optical parameters is simplified to a constrained optimization problem.

Numerical Method: With the generalized Delta-Eddington phase function, we have the following phase approximation equation to RTE with excitation light source on the boundary of object:

$$\Phi(\mathbf{r}) = \frac{1}{4\pi}\int_{\Omega} \hat{\mu}_s(\mathbf{r}')\Phi(\mathbf{r}')G(\mathbf{r},\mathbf{r}')d\mathbf{r}' - \int_{\partial\Omega}\left[\frac{r_d}{4\pi(1+r_d)}\Phi(\mathbf{r}') + S(\mathbf{r}')\right]G(\mathbf{r},\mathbf{r}')\beta\cdot n d\mathbf{r}' \qquad (3\text{-}6)$$

where $\hat{\mu}_s(\mathbf{r}') = (1-f)\mu_s$ is the reduced scattering coefficient, and $\hat{\mu}_t(\mathbf{r}') = \mu_a(\mathbf{r}') + \hat{\mu}_s(\mathbf{r}')$ is the reduced attenuation coefficient.

$$G(\mathbf{r},\mathbf{r}') = \frac{1}{|\mathbf{r}-\mathbf{r}'|^2}\exp\left(-\int_0^{|\mathbf{r}-\mathbf{r}'|}\hat{\mu}_t(\mathbf{r}')(\mathbf{r}'-t\beta)dt\right), \qquad (3\text{-}7)$$

and $\beta = \dfrac{\mathbf{r}-\mathbf{r}'}{|\mathbf{r}-\mathbf{r}'|}$, $S(\mathbf{r})$ is a collimated illumination source on the boundary, and r_d is the internal reflection coefficient that is approximated by

$$r_d = -1.4399\eta^{-2} + 0.7099\eta^{-1} + 0.6681 + 0.0636\eta, \quad \eta = n_{tissue}/n_{air}\,. \qquad (3\text{-}8)$$

To compute the photon fluence rate from Eq. (2-21), the region of interest Ω is discretized into finite elements with N vertex nodes and the photon fluence rate $\Phi(\mathbf{r})$ is approximated in terms of nodal-based basis functions $\varphi_j(\mathbf{r})\ (j=1,2,\cdots,N)$,

$$\Phi(\mathbf{r})=\sum_{j=1}^{N}\Phi(\mathbf{r}_j)\varphi_j(\mathbf{r}). \tag{3-9}$$

Substituting Eq. (3-9) into Eq. (3-6), we obtain the following matrix equation

$$\{\mathbf{\Phi}\}=\mathbf{M}\{\mathbf{\Phi}\}+\mathbf{B}\{\mathbf{\Phi}\}+\{\mathbf{S}\}, \tag{3-10}$$

where $\{\mathbf{\Phi}\}$ consists of photon fluence rate values at the nodes in Ω; $\mathbf{M}$, $\mathbf{B}$ and $\{\mathbf{S}\}$ represent the corresponding discrete integral kernels in Eq. (3-6), with the components of the matrices defined by

$$\begin{cases} m_{i,j}=\dfrac{1}{4\pi}\displaystyle\int_{\Omega}\hat{\mu}_s(\mathbf{r}')\varphi_j(\mathbf{r}')G(\mathbf{r}_i,\mathbf{r}')\mathbf{dr}' \\ b_{i,j}=\dfrac{r_d}{4\pi(1+r_d)}\displaystyle\int_{\Omega}\varphi_j(\mathbf{r}')G(\mathbf{r}_i,\mathbf{r}')(\boldsymbol{\beta}\cdot\mathbf{n})\mathbf{dr}' \\ s_i=\dfrac{1}{4\pi}\displaystyle\int_{\Omega}S(\mathbf{r}')G(\mathbf{r}_i,\mathbf{r}')\mathbf{dr}' \end{cases}. \tag{3-11}$$

Eq. (2-24) can be expressed as

$$\mathbf{K\Phi}=\mathbf{S} \tag{3-12}$$

where $\mathbf{K}=(\mathbf{I}-\mathbf{M}-\mathbf{B})$. The integrals are evaluated using the Gauss-Legendre quadrature rule. Singular points in the quadrature need to be handled to ensure the numerical accuracy of the solution. The singularities occur at $r_i=r'$, which are the vertices of each tetrahedral element. We denote the vertices of a tetrahedron as (x_1,y_1,z_1), (x_2,y_2,z_2),

$(x_3, y_3, z_3), (x_4, y_4, z_4)$. Without losing generality, let us only show the case $r_i = (x_4, y_4, z_4)$. We integrate over an arbitrary tetrahedron by performing an integral over the unit orthogonal tetrahedron in volume coordinate (ξ, η, ζ) after the transformation,

$$\begin{cases} x(\xi,\eta,\zeta) = x_4 + \xi(x_1 - x_4) + \eta(x_2 - x_4) + \zeta(x_3 - x_4) \\ y(\xi,\eta,\zeta) = y_4 + \xi(y_1 - y_4) + \eta(y_2 - y_4) + \zeta(y_3 - y_4) \\ z(\xi,\eta,\zeta) = z_4 + \xi(z_1 - z_4) + \eta(z_2 - z_4) + \zeta(z_3 - z_4) \end{cases} \tag{3-13}$$

where the singular point (x_4, y_4, z_4) is mapped to the origin of the volume coordinate system. To avoid the singular point, the integral is expressed in a spherical coordinate system:

$$\begin{aligned} m_{i,j} &= \frac{\hat{\mu}_s |\det J|}{4\pi} \int_{\Omega} \frac{\phi_j}{\lambda} \exp\left(\hat{\mu}_t \rho \sqrt{\lambda}\right) \sin\phi \, d\rho \, d\theta \, d\phi \\ &= \frac{\hat{\mu}_s |\det J|}{4\pi} \int_0^{\frac{\pi}{2}} \int_0^{\frac{\pi}{2}} \int_0^{\frac{1}{\tau}} \frac{\phi_j}{\lambda} \exp\left(\hat{\mu}_t \rho \sqrt{\lambda}\right) \sin\phi \, d\rho \, d\theta \, d\phi \end{aligned} \tag{3-14}$$

where

$$\tau = \cos\theta \sin\phi + \sin\theta \sin\phi + \cos\phi$$

and

$$\begin{aligned} \lambda = &\left[(x_1 - x_4)\cos\theta \sin\phi + (x_2 - x_4)\sin\theta \sin\phi + (x_3 - x_4)\cos\phi\right]^2 + \\ &\left[(y_1 - y_4)\cos\theta \sin\phi + (y_2 - y_4)\sin\theta \sin\phi + (y_3 - y_4)\cos\phi\right]^2 + \\ &\left[(z_1 - z_4)\cos\theta \sin\phi + (z_2 - z_4)\sin\theta \sin\phi + (z_3 - z_4)\cos\phi\right]^2 \end{aligned}$$

Iterative Optical Parameter Identification: With the correct optical parameters, the calculated photon fluence rate from the PA model will be a good approximation to the surface measurement. The optical parameter identification process is to minimize the difference between model prediction and surface measurement by updating the optical parameters iteratively, and can be expressed as the following minimization problem:

$$\left(\mu_a, \hat{\mu}_s\right) = \arg\min\left[\left(\Phi^m - \Phi^p\left(\mu_a, \hat{\mu}_s\right)\right)^T \left(\Phi^m - \Phi^p\left(\mu_a, \hat{\mu}_s\right)\right)\right] \tag{3-15}$$

where Φ^m is the photon fluence rate measurement at the surface and Φ^p is the photon fluence rate predicated by the PA model. We use the conjugate gradient (CG) optimizer to solve Eq. (3-15). The gradient of objective function Ψ is calculated using adjoint differentiation:

$$\frac{\partial \Psi}{\partial \mu_x} = 2\left(\Phi^m - \Phi^p\left(\mu_a, \hat{\mu}_s\right)\right) K^{-1}\left(\frac{\partial K}{\mu_x}\Phi^p\left(\mu_a, \hat{\mu}_s\right) - \frac{\partial S}{\partial \mu_x}\right) \tag{3-16}$$

CG optimization starts from an arbitrary initial guess of optical parameters. However, the CG minimization procedure is sensitive to the initial optical parameters, and a poor selection of the initial guess will lead to a local minimum instead of the true solution [68]. To improve the robustness of the optimization, the CG method can be preceded by a global search procedure. The global search is used to provide the CG optimizer with a good initial solution, which is close to the true solution. Thus, the CG method will much more likely converge to the true solution. Differential evolution (DE) is a population-based stochastic method for global optimization. In DE, the collection of solution vectors is called the population which is denoted as

$$P_{x,g} = \left\{x_{i,g}\right\}, \quad i = 1, 2, \cdots, N_p, \quad g = 1, 2, \cdots, g_{\max} \tag{3-17}$$

where N_p is the population size, and g the number of generations. The solution vector in this case consists of the optical parameters: $\mathbf{x} = (\mu_a, \hat{\mu}_s)$. The population is mutated using the unique differential operator:

$$\mathbf{v}_{i,g} = \mathbf{x}_{r_0,g} + F(\mathbf{x}_{r_1,g} - \mathbf{x}_{r_2,g}) \tag{3-18}$$

where F is the difference scale factor, which is the most important control parameter of DE. The base vector $\mathbf{x}_{r_0,g}$ and the difference vectors $\mathbf{x}_{r_1,g}$ and $\mathbf{x}_{r_2,g}$ are randomly selected but r_0, r_1, and r_2 should be mutually exclusive. The mutated vector $\mathbf{v}_{i,g}$ then exchanges information with a target vector $\mathbf{y}_{i,g}$ which is selected sequentially from the population to generate a trial vector $\mathbf{u}_{i,g}$: each component in the trial vector inherits from that of the mutated vector if a binomial trial is a success, i.e. $rand[0,1) \le Cr$, where Cr is the crossover rate; otherwise, that component will inherit from the target vector. If the trial vector is a better solution, i.e., it has a smaller objective function value, then the trial vector replaces the target vector in the population. Finally, the generation counter is advanced when the entire population is updated, and the solution vector with the smallest function value is used as the solution when the maximum generation is reached. The solution generate by the DE optimization in a small number of iterations is used as the initial starting point for the CG optimizer. Using this hybridization scheme, we can enhance the likelihood of finding the true solution when the *a priori* knowledge on the optical properties is uncertain.

Experiments and Results: First we characterize the accuracy of our algorithm using simulated measurements. The simulations are performed on a digital phantom of

10mm×10mm×10mm cube with four different optical property configurations. An illumination source was set on one side of the cube and emitted a pencil beam of 1μW into the phantom. Monte Carlo (MC) simulation was used to generate the measurements on the opposite side of the source. Because of the intrinsic Poisson noise in MC simulated, no additional noise is added. The simulated measurements are presented in Figure 3-3.

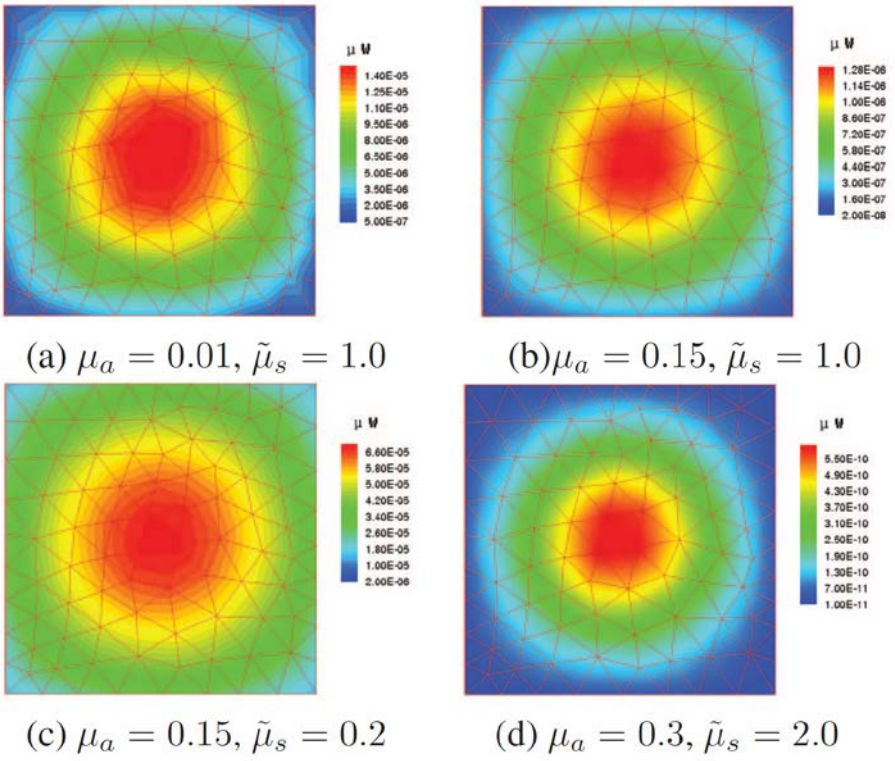

Figure 3-3. *Simulated measurements of four optical property configurations.*

To apply the reconstruction algorithm, we generated a finite element model for the slab. The finite element model was composed of 1708 nodes and 8665 tetrahedron with average edge length of 1.0mm. We used a population size of 24, differential scale factor of 0.8, and crossover rate of 0.9 for the differential evolution optimization and allow maximum20 generations and selected the single best candidate solution from the

population as the starting point of the conjugate gradient optimizer. The reconstruction results are listed in Table 3-1.The relative error for the reconstruction of μ_a is less than10% and the error for $\hat{\mu}_s$ is less than 6%.

Table 3-1. Reconstructed Optical Parameters

True		Reconstructed	
$\mu_a \left(mm^{-1}\right)$	$\hat{\mu}_s \left(mm^{-1}\right)$	$\mu_a \left(mm^{-1}\right)$	$\hat{\mu}_s \left(mm^{-1}\right)$
0.01	1.0	0.0098	1.012
0.15	1.0	0.161	0.979
0.15	0.2	0.152	0.197
0.30	2.0	0.273	2.118

Using the optical property identification algorithm, we estimated the optical parameters of a mouse-shaped phantom (Xenogen Corporation) for different light spectra. The phantom material was homogeneous and an illumination light source (Xenogen XPM-2) was embedded. The light source can be treated as a point source and has a depth of 4.8mm to the bottom surface of the mouse phantom. Using two filters of 515-575nm and 575-650nm, we obtain two sets of measurement of the photons escaping from the flat surface of the phantom using Xenogen's IVIS 100 series imaging system, respectively. A finite element model was established from the microCT image volume of the mouse-shaped phantom. The finite element model had 3864 nodes and 14708 tetrahedra. The measurements were mapped to the corresponding surface of the finite element model, as in Figure 3-4.

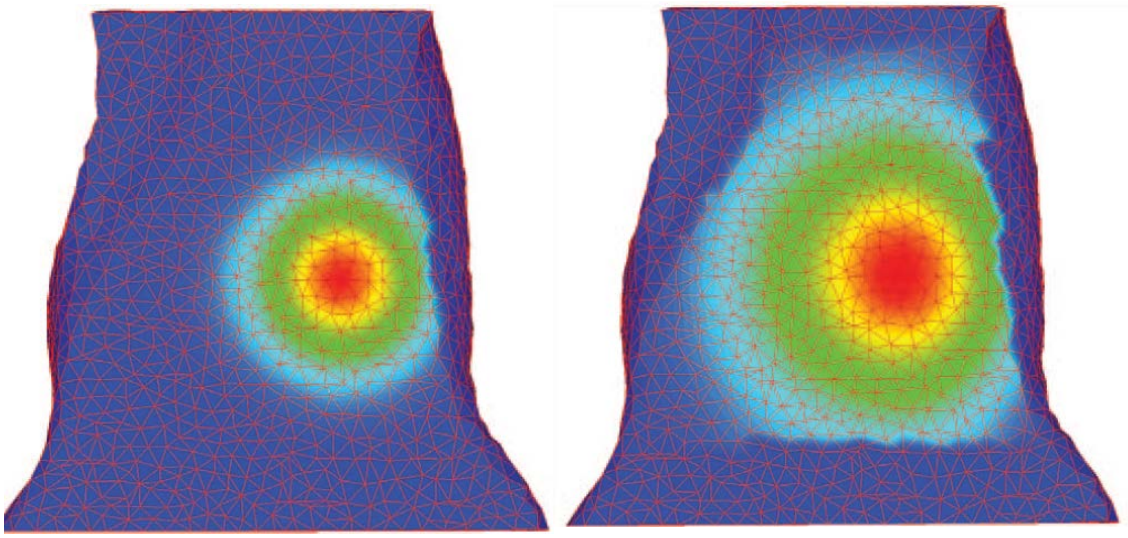

Figure 3-4.*The measurements (left: GFP, right: DsRed) mapped to the surface nodes of the mouse finite element model.*

To reconstruct the optical parameters under each spectrum, we used a population size of 24, differential scale of 0.8, crossover rate of 0.5, and maximum generation of 20 for the differential evolution optimization before the CG optimizer. The reconstructed optical properties are listed in Table 3-2.

Table 3-2. Reconstructed Optical Parameters For Two Illumination Spectra

Spectrum (nm)	$\mu_a \left(mm^{-1}\right)$	$\hat{\mu}_s \left(mm^{-1}\right)$
515 – 575	0.1127	1.625
575 – 650	0.0167	1.551

Optical property estimation based on the PA model will inherently yield accurate optical parameters for a wide range of tissue properties. The accuracy of the optical parameters characterization, however, does not solely depend on the accuracy of the forward model; the iterative algorithm could converge prematurely to an inaccurate solution if the initial

guess is not close enough to the true solution. Fortunately, differential evolution is an effective global search method to find a good starting point quickly. The iterative procedure is robust to noise data and can eliminate the need of initial guess of the optical parameters. The proposed optical property characterization method, along with the PA model will improve the accuracy for optical molecular imaging modalities.

Chapter 4. Finite Element Reconstruction

The reconstruction algorithms of light sources are to localize and quantify molecular probe distribution in 3-D from light intensity measurement on surface of object. Owing to the high degrees of absorption and scattering of light through tissue, the reconstruction of lighting molecular probes is inherently ill-posed, commonly leading to nonunique solutions and aberrant reconstruction in the presence of measurement noise and optical parameter mismatches. Researchers have invested considerable effort to obtain stable solutions for the reconstruction. Tikhonov regularization is often used to alleviate the ill-posed nature of this problem [16, 69]. We developed a reconstruction method using multispectral measurements [70]. The numerical experiments show that multispectral measurements improve the spatial resolution of reconstructed images.

Section 4.1. Source Reconstruction Based on Diffusion Approximation

The diffusion approximation equations (2.1)-(2.2) with respect to $\Phi(\mathbf{x})$ can be equivalently represented as the following weak form [53],

$$\begin{aligned}\int_{\Omega}\Big(D(\mathbf{x})\big(\nabla\Phi(\mathbf{x})\big)\cdot\big(\nabla\Psi(\mathbf{x})\big)+\mu_a(\mathbf{x})\Phi(\mathbf{x})\Psi(\mathbf{x})\Big)\mathrm{d}\,\mathbf{x}\\ +\int_{\partial\Omega}\Phi(\mathbf{x})\Psi(\mathbf{x})\Big/\big(2A(\mathbf{x};n,n')\big)\mathrm{d}\,\mathbf{x}=\int_{\Omega}S(\mathbf{x})\Psi(\mathbf{x})\mathrm{d}\,\mathbf{x}\end{aligned} \tag{4-1}$$

for an arbitrary test function $\Psi(\mathbf{x})$. Following the standard finite-element method [20], Ω is discretized with T vertex nodes $(N_1, N_2, ..., N_T)$ and N_e elements, denoted as $\Omega^{(l)}$ $(l = 1, 2, ..., N_e)$, such that $\Omega = \bigcup_{l=1}^{N_e}\Omega^{(l)}$. Then $\Phi(\mathbf{x})$ can be approximated with a piecewise polynomial function [53],

$$\Phi(\mathbf{x}) \approx \Phi^{\mathrm{h}}(\mathbf{x}) = \sum_{k=1}^{T} \phi_k \varphi_k(\mathbf{x}) \quad \text{when } \mathbf{x} \in \Omega, \tag{4-2}$$

where ϕ_k is the nodal value of $\Phi(\mathbf{x})$ on the k-th node N_k; and $\varphi_k(\mathbf{x})$ the nodal basis function with support over the elements $\Omega^{(l)}$, which have the node N_k as a common vertex, that is $\mathrm{supp}(\varphi_k(\mathbf{x})) = \cup_{N_k \in \Omega^{(l)}} \Omega^{(l)}$. Similarly, the source function $S(\mathbf{x})$ is approximated as [20],

$$S(\mathbf{x}) \approx S^h(\mathbf{x}) = \sum_{k=1}^{N_s} S_k \gamma_k(\mathbf{x}) \quad \text{when } \mathbf{x} \in \Omega \tag{4-3}$$

where S_k are the discrete values of $S(\mathbf{x})$, and $\gamma_k(\mathbf{x})$ are the interpolation basis functions $(k = 1, 2, ..., N_s)$; N_s is the number of interpolation basis functions for the source. Inserting Eqs. (4-2) - (4-3) into Eq. (4-1) and using the nodal basis functions $\varphi_k(\mathbf{x})$ $(k = 1, 2, ..., T)$ as the test functions, we obtain the following matrix equation

$$\left([\mathrm{K}] + [\mathrm{C}] + [\mathrm{B}]\right)\{\Phi\} = [\mathrm{M}]\{\Phi\} = [\mathrm{F}]\{S\}, \tag{4-4}$$

where the components of the system matrices are given by

$$\begin{cases} k_{ij} = \int_{\Omega} D(\mathbf{x}) \left(\nabla \varphi_i(\mathbf{x})\right) \cdot \left(\nabla \varphi_j(\mathbf{x})\right) \mathrm{d}\mathbf{x} \\ c_{ij} = \int_{\Omega} \mu_a(\mathbf{x}) \varphi_i(\mathbf{x}) \varphi_j(\mathbf{x}) \mathrm{d}\mathbf{x} \\ f_{ij} = \int_{\Omega} \varphi_i(\mathbf{x}) \gamma_j(\mathbf{x}) \mathrm{d}\mathbf{x} \\ b_{ij} = \int_{\partial\Omega} \varphi_i(\mathbf{x}) \varphi_j(\mathbf{x}) / \left(2A(\mathbf{x}; n, n')\right) \mathrm{d}\mathbf{x} \end{cases} \tag{4-5}$$

According to the convergence theorem for the finite element method [9, 21], the solution of Eq. (4-4) converges to the exact continuous solution of the diffusion equation (1) when the maximum size of the elements approaches zero. In the inverse source reconstruction,

mesh sizes and shape functions should be chosen to balance the accuracy and the computational efficiency.

To describe the inverse source reconstruction method, we rewrite Eq. (4-4) as

$$\begin{bmatrix} \mathrm{M}_{11} & \mathrm{M}_{12} \\ \mathrm{M}_{12}^{T} & \mathrm{M}_{22} \end{bmatrix} \begin{Bmatrix} \Phi^{m} \\ \Phi^{*} \end{Bmatrix} = \begin{bmatrix} \mathrm{F}_{11} & \mathrm{F}_{12} \\ \mathrm{F}_{21} & \mathrm{F}_{22} \end{bmatrix} \begin{Bmatrix} S^{p} \\ S^{*} \end{Bmatrix}, \tag{4-6}$$

where Φ^{m} represents the measurable nodal photon density on the boundary $\partial\Omega$, and Φ^{*} the photon density on internal nodes. In our experiments, Φ^{m} is computed from the surface flux image captured with a CCD camera. The source vector S is divided into two parts: S^{p} in the permissible source region Ω_{s} and S^{*} in the forbidden region. Clearly, S^{*} is zero by definition. Note that the permissible source region Ω_{s} must be selected to be sufficiently large to contain the actual source region where the reporter genes may present. The sub-metrics, M_{11}, M_{12} and M_{22} of M and F_{11}, F_{12}, F_{21} and F_{22} of F, are arranged in consistence with S^{p}, S^{*}, Φ^{m} and Φ^{*}. Thus, Eq. (4-6) can be reduced to

$$\left(\mathrm{M}_{11} - \mathrm{M}_{12}\,\mathrm{M}_{22}^{-1}\,\mathrm{M}_{12}^{T}\right)\Phi^{m} = \left(\mathrm{F}_{11} - \mathrm{M}_{12}\,\mathrm{M}_{22}^{-1}\,\mathrm{F}_{21}\right)S^{p}. \tag{4-7}$$

Since the matrix M is symmetric and positive definite, Φ^{m} can be uniquely determined from

$$\mathbf{\Phi}^{m} = \mathbf{M} \cdot \mathbf{S}^{p}, \tag{4-8}$$

assuming that the source S^{p} is known, where $\mathbf{M} = \left(\mathrm{M}_{11} - \mathrm{M}_{12}\mathrm{M}_{22}^{-1}\mathrm{M}_{12}^{\mathrm{T}}\right)^{-1}\left(\mathrm{F}_{11} - \mathrm{M}_{12}\mathrm{M}_{22}^{-1}\mathrm{F}_{12}^{\mathrm{T}}\right)$. In an optical imaging experiment, the photon fluence rate $\mathbf{\Phi}^{m}$ on the object surface can be measured with a CCD camera.

Hence, The inverse source reconstruction is reduced to solve the linear system of equation (4-8) with respect to $\mathbf{S}^{\mathbf{p}}$ from measured $\mathbf{\Phi}^{m}$.

Theoretically, measured photon fluence rate is two-dimensional, light sources distribute in three-dimensional region, and the inverse source is underdetermined. An effective way to reduce the number of unknown variables is to impose permissible source regions [16]. Optical imaging views taken by a CCD camera indicate high-value clusters, and prominent high-density clusters should be closer to sources than other surface places. In some cases, permissible source regions can be also outlined based on prior knowledge. With these hints it is easy to generate permissible source regions where light sources may exist. Additionally, an adaptive procedure can efficiently determine permissible source regions: an initial permissible source region can be given to perform the reconstruction on a low resolution scale, and high values of reconstructed sources will be very likely located in a neighbor of or within real light sources. Then, the permissible source regions can be updated in reference to these highly valued nodes. Applying the permissible source region can significantly reduce the number of unknown variables and enhance the stability of the reconstruction.

Section 4.2. Multispectral Reconstruction

Bioluminescent spectral analysis experiment shows that the molecular probes typically emit broader spectral range, and multiple spectral measurements can be performed in the optical imaging experiment using optical filters [18, 69-71]. The four kinds of luciferase enzymes hRLuc, CNGr68, Fluc+, and CBRed have different emission peaks at 480 nm, 543 nm, 612 nm, and 615 nm, respectively, as shown in Figure 4-1. Their fusion creates

broad emission spectra. The spectral properties of the luciferase light source should have a significant impact on how much of the light is transmitted to the external surface. The detected photon densities at different energy bins carry more information about the bioluminescence source than the corresponding integrated signals. In practice, the spectral distribution of a specific molecular probe can be well measured in Laboratory. Hence, the proportion factor for each spectral band to total source power can be obtained, and the source's total power can be decomposed into a weighted sum of energy from each spectrum:

$$S = \sum_{\tau=1}^{T} w_\tau S_\tau \tag{4-9}$$

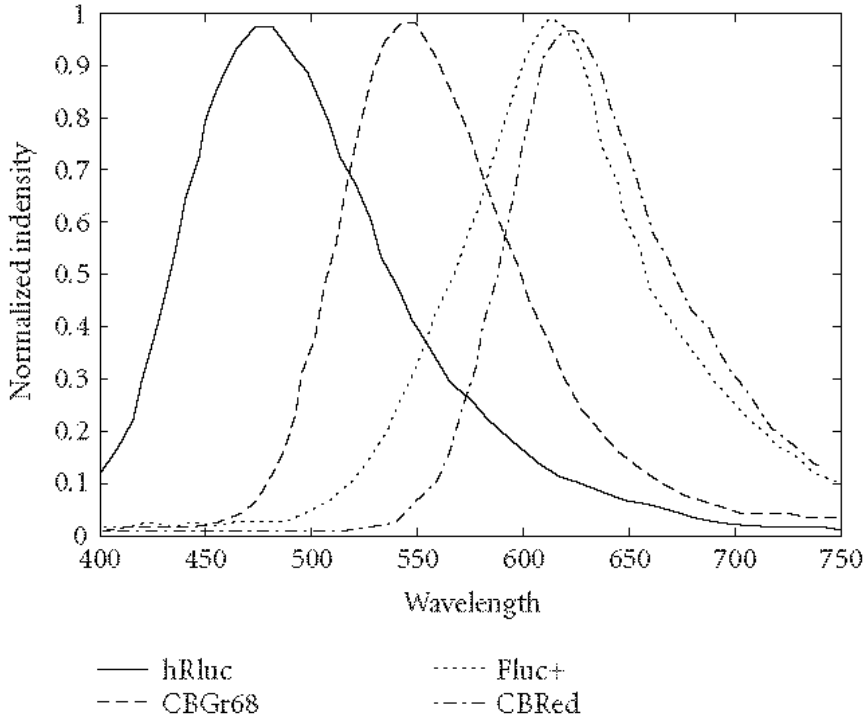

Figure 4-1: *Spectral distributions of luciferase enzymes measured using spectrometry.*

The multi-spectral information can enhance the stability and accuracy of reconstruction. Hence, Eq. (4-8) can be modified to a multi-spectral linear system of equations,

$$\begin{bmatrix} w_1\mathbf{M}_1 \\ w_2\mathbf{M}_2 \\ \vdots \\ w_T\mathbf{M}_T \end{bmatrix}\mathbf{S} = \begin{bmatrix} \Phi_1^m \\ \Phi_2^m \\ \vdots \\ \Phi_T^m \end{bmatrix} \tag{4-10}$$

where $\mathbf{M}_k$, $(k = 1,2,\cdots,T)$ is system matrix for each spectral band and rely on the spectrum-specific optical parameters μ_a and μ_s. Because the measured data are typically corrupted by noise, it is not optimal to solve Eq. (4-10) directly. In generally, optimization algorithm is often used to find an optimal solution,

$$\hat{\mathbf{S}} = \arg\min \sum_{k=1}^{T} \left\| w_k\mathbf{M}_k - \Phi_k^m \right\| + \alpha R(\mathbf{S}) \tag{4-11}$$

where $R(\mathbf{S})$ is a stabilizing function, and α the regularization parameter. Several standard optimization methods can be used to solve Eq. (4-11), for example, a modified Newton method and an active set strategy for bound constrained optimization isan effective method to solve the minimization problem to determine light source distribution [13, 16].

Section 4.3. Numerical Studies

Single-band reconstruction: The numerical simulation was performed using a heterogeneous numerical phantom that contains regions resembling lungs, heart, muscle, and bone. This cylindrical phantom had a diameter of 30mm and height of 26 mm, as shown in Figure 4-2 (a). The phantom was discredited into 6576 vertex nodes and 11340 prism elements. The two bioluminescent sources were embedded in the left lung, as

shown in Figure 4-2(b). The first source was located at (−8.66, 3.46, 13.10), while the second one at (−10.21, −3.17, 13.10). Both sources had photon density of 300pW/mm3. The permissible region was selected based on a priori knowledge, as shown in Figure 4-2(c). This region contained 308 elements. The optical parameters averaged over the spectral range [400 nm, 750 nm] for each type of structure in the heterogeneous phantom are listed in Table 4-1. The simulated measurement data on the 1024 detector points on side surface of the phantom were generated according to the finite-element forward model. Then, the measurement data were corrupted with 20% Gaussian noise to simulate measurement errors. We set the stabilizing function $R(\mathbf{S}) = \mathbf{S}^T\mathbf{S}$ and the regularization parameter $\alpha = 3.0 \times 10^{-8}$, and then performed the source reconstruction using the single-band BLT algorithm. The reconstructed locations of the sources are shown in Figure 4-3(a). The photon densities of the sources are shown in Figure 4-4(a). The quantitative data on the reconstruction are listed in Table 4-2.

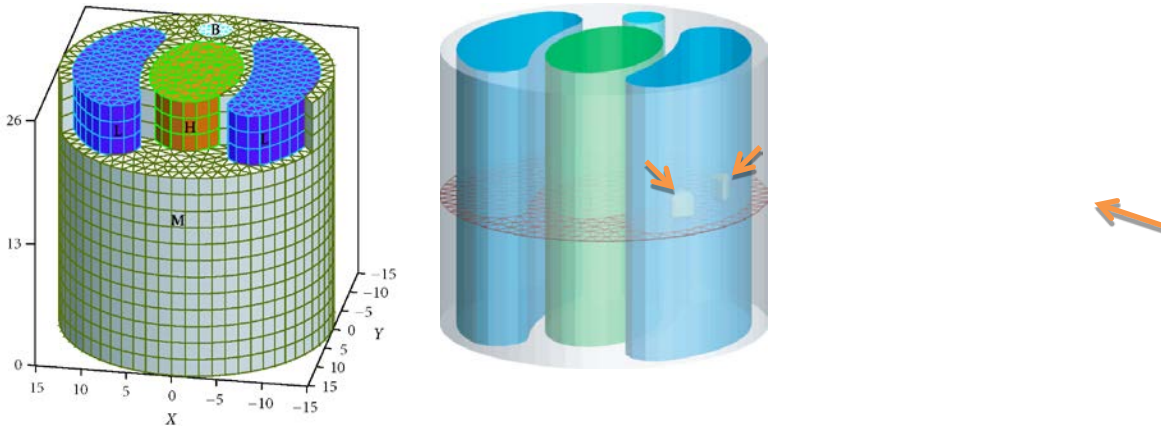

(a) (b) (c)

Figure 4-2. *Heterogeneous mouse chest phantom with regions represent the lungs (L), bone (B), heart (H), and muscle (M). (a) Phantom geometry; (b) Source distribution in numerical simulation; (c) Source permissible region in numerical simulation.*

Multiband reconstruction: We performed the proposed multispectral BLT reconstruction using the same numerical model described in Section 3.2. According to the literature [19, 20], various optical parameters (absorption, scattering) were assigned to different regions of the numerical heterogeneous phantom, as listed in Table 3. Three measurement data sets on the 1024 detector points on the phantom side surface were similarly generated for spectral ranges [400 nm, 530 nm], [530 nm, 630 nm], and [630 nm, 750 nm], respectively. The data sets were also corrupted with 20% Gaussian noise. With the same definition for the stabilizing function and the regularization parameter in above Section, the three simulated spectral datasets were taken into the multiband/multispectral reconstruction of the source distribution using our method described in above Section. The reconstructed locations of the sources are shown in Figure 4-3(b). The photon densities of the sources are shown in Figure 4-4(b). The multiband reconstruction is quantitatively compared to the single-band reconstruction in Table 4-2. Both source locations were correctly reconstructed, and the maximum relative source power error was 35%. The reconstructed results of multispectral BLT are clearly superior to those of single-spectral BLT. The proposed multiband reconstruction method greatly increases the measurement information, effectively reduces the ill-posedness of BLT, and significantly improves the accuracy and stability of the bioluminescent source reconstruction.

Table 4-1. Optical Parameters of Each Component in the Phantom

Region	$\mu_a \left(mm^{-1}\right)$	$\mu_s' \left(mm^{-1}\right)$
Muscle	0.0068	1.081
Lung	0.0233	1.974
Heart	0.0104	1.008
Bone	0.0001	0.060

Table 4-2: Reconstruction results obtained using the single-band and multiband algorithms.

Source	Single-band reconstruction		Multiband reconstruction	
	Position Relative error	Photon density (pW/mm^3)	Position Relative error	Photon density (pW/mm^3)
Source-I	183.06	39.0%	195.69	34.8%
Source-II	194.58	35.1%	236.12	21.3%

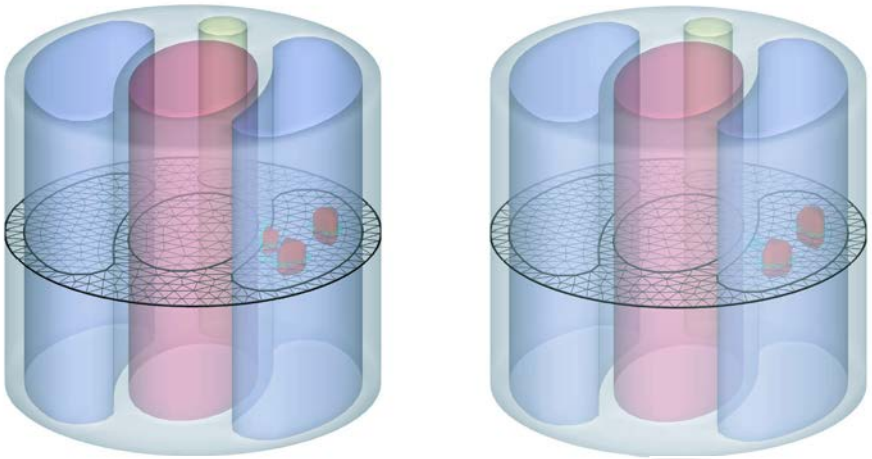

(a) (b)

Figure 4-3: *Single-band and multispectral reconstructions. (a) The source distribution reconstructed using the single-band algorithm, and (b) the counterpart reconstructed using the multispectral algorithm.*

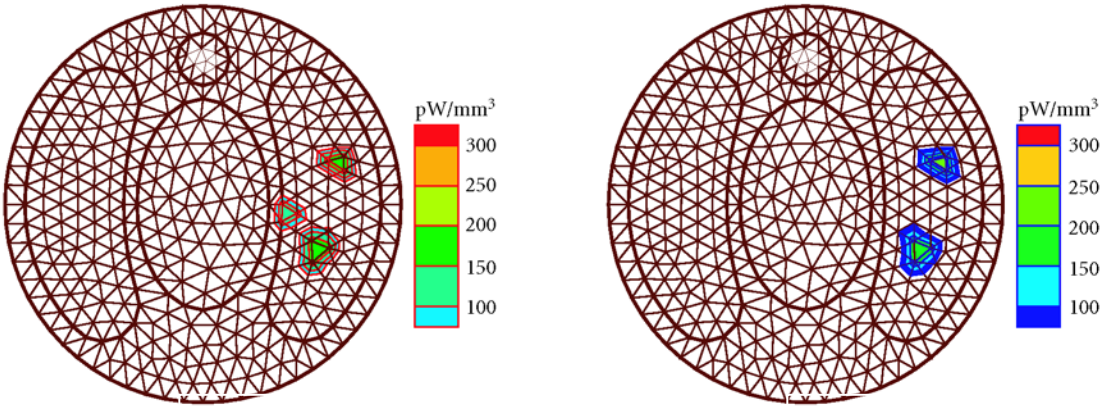

(a) (b)

Figure 4-4: *Source densities in the single-band and multispectral reconstructions. (a) The source density reconstructed using the single-band algorithm, and (b) the counterpart reconstructed using the multispectral algorithm.*

Chapter 5. Well-posed Inverse Source Model and Reconstruction

In this research, we develop a new inverse source model, and differential evolution-based reconstruction algorithm to determine the source locations and strengths accurately and reliably. The new model is well-posed, and has an unique and stable solution [20]. We developed a differential evolution (DE)-based heuristic reconstruction algorithm to solve the inverse source problem by incorporating the number of light sources as constraint in its encoding scheme. DE is based on a spontaneous self-adaptive vector difference operator, and displayed a superior converging behavior with a high precision. Furthermore, we proposed an iterative method to estimate the number of isolated sources. This novel method greatly enhances the accuracy and stability of the reconstruction [20].

Section 5.1. Well-posed Inverse Source Model

Many in vivo studies involve small and isolated bioluminescent sources, such as small tumor sites in mouse tumor model. The photon propagation in biological tissues is highly scattering and multiple scattering events occur around 1 mm from the source. So, a small-size light source is blurred with the multi-scattering event to a sphere from the external observation. In this case, the actual shape of the source cannot be retrieved from the measured diffused signal on the surface. The location and power of a bioluminescence source are the characteristics of interest [12, 72, 73], which can be equivalently represented as a point source. The distribution of a finite number of light sources is expressed as follows:

$$S(\mathbf{r}) = \sum_{i=1}^{N} w_i \delta(\mathbf{r} - \mathbf{r}_i) , \tag{5-1}$$

where N is the number of light sources, w_i is the power of i-th source, $\mathbf{r}_i$ is the position of i-th source. We defined a new regularized model as: given the optical parameters μ_a and μ_s of each subdomain Ω_s in domain Ω and the number of isolated light sources S in the interior of the Ω, the inverse source problem is to reconstruct the positions $\{\mathbf{r}_i \quad (i=1,2,\cdots,N)\}$ and powers $\{w_i \quad (i=1,2,\cdots,N)\}$ of the light sources from the diffused light signal at the boundary of the object. The solution uniqueness of the inverse source problem is guaranteed by the following theorem:

Theorem 5.1 ([74, 75]): If $S(\mathbf{r})=\sum_{i=1}^{N} w_i \delta(\mathbf{r}-\mathbf{r}_i)$ and $S'(\mathbf{r})=\sum_{i=1}^{N} w_i' \delta(\mathbf{r}-\mathbf{r}_i')$ are two solutions to the inverse source problem, then there is a permutation τ of $\{1,2,\cdots,N\}$ such that $w_i' = w_{\tau_i}$ and $\mathbf{r}_i' = \mathbf{r}_{\tau_i}$.

Based on the new model, the traditional inverse source reconstruction can be converted to the following constrained optimization problem:

$$\min_{s_{i_1}>0,\cdots,s_{i_k}>0} \|\mathbf{AS}-\mathbf{\Phi}\| \tag{5-2}$$

S only includes k positive nonzero values $\{s_{i_1}, s_{i_2}, \cdots, s_{i_k}\}$ which represent the power of the point sources, while the remaining components of S are zeros, i.e., the number of sources is known to be k. The position of a positive nonzero value in the vector S corresponds to its node index in the finite-element mesh, from which the Cartesian coordinates of the point sources are obtained. The new reconstruction model based on Eq. (5-2) has a unique solution, and can effectively overcome the ill-posedness of bioluminescence tomography. The optimization problem (5-2) is which is non-deterministic polynomial time hard (NP-hard), and cannot be efficiently solved using

conventional gradient-based optimization methods. In this work, we present a heuristic method based on DE optimization technique to solve the optimization problem.

Section 5.2. Differential Evolution Based Solution

The conventional deterministic optimization methods, like gradient-guided optimization schemes have two major drawbacks for solving the optimization problem presented in Eq. (5-2): the difficulty to incorporate the complex constraints and the inability to find the global optimal solution. Although the regularized model (5.2) has a unique global optimal solution, many local optimal solutions may exist, especially in the presence of noise, inaccurate optical parameters and physical model. The local optimal solution is suboptimal and may have poor accuracy; therefore, a powerful global optimizer is desired to avoid locally optimal solutions of the regularized model. After surveying several optimization methods, we adopted a DE algorithm. DE is based on a spontaneous self-adaptive vector difference operator [20, 76-78], and displayed superior convergence behavior and high numerical precision. Numerous benchmark and real-life problems reported that the DE often has the fastest and most reliable convergence behavior with a comparatively small population size [79].

Unlike most deterministic optimization methods, which operate on a single point, DE operates on multiple points in order to sample globally, encoding each candidate solution as a real valued vector. This representation gives DE great versatility and the ability to handle the number of sources constraint intrinsically. Using the inverse source model, a candidate solution $\mathbf{S}$ for the light source reconstruction is expressed as N quadruples

$$\mathbf{S} = \{\mathbf{s}_1, \mathbf{s}_2, \cdots, \mathbf{s}_N\} \tag{5-3}$$

where $\mathbf{s}_i = (x_i, y_i, z_i, w_i)$ describes the i-th point source location in the Cartesian coordinate and its power. Each quadruple s_i is subjected to the same boundary constraint

$$\mathbf{s}_l \le \mathbf{s}_i \le \mathbf{s}_u \tag{5-4}$$

The point source coordinate is limited by the dimension of the finite-element model and the source power ranges from zero to an empirically determined value. A collection of solution vectors $\{\mathbf{S}_1, \mathbf{S}_2, \cdots, \mathbf{S}_P\}$ forms a population of size P that samples the search space in an evolutionary fashion. The first step of DE is to initialize the population randomly. Each quadruple $\mathbf{s}$ in a solution vector $\mathbf{S}$ is initialized as follows:

$$\mathbf{s} = \left(\langle x_l, x_u \rangle, \langle y_l, y_u \rangle, \langle z_l, z_u \rangle, \langle w_l, w_u \rangle\right) \tag{5-5}$$

where $\langle \circ, \circ \rangle$ denotes the uniform distribution between lower and higher values. This uniformly distributed initial population uses no knowledge of the location of the global optimum within the boundaries; therefore, the optimization does not depend on initial starting point. From an evolutionary algorithms point of view, the uniform initialization introduces diversity to reduce the probability of premature convergence.

DE belongs to a class of population-based stochastic optimization methods [20, 76, 77], which share a common structure, as illustrated in Fig. 5.1. DE got its name from its special vector difference operator, which is of paramount importance to the algorithm. The vector difference operator has a very simple form

$$\mathbf{U} = \mathbf{S}_{r0} + F \cdot (\mathbf{S}_{r1} - \mathbf{S}_{r2}) \tag{5-6}$$

where $\mathbf{U}$ is the generated trial vector, r_0 is the index of the base vector, r_1 and r_2 are the indices of the difference vectors, F is the difference scaling factor. The trial vector may

replace a target vector with index i. Indices i, r_0, r_1, r_2 must be mutually exclusive. The index i is selected in an ordered fashion from 1 to *P*. The base vector index r_0 is selected in order from a permuted sequence $\tau = \{1, 2, \cdots, P\} - \{i\}$ and the difference vector indices r_1 and r_2 are randomly selected from the set $\{1, 2, \cdots, P\} - \{i, r_0\}$. The control parameter of this operator is *F*, which determines how much perturbation of the vector difference to add to the base vector. *F* has an empirically determined bound between [0, 1], and should use a larger value with a smaller population size and vice versa. Adding a scaled vector difference to the base vector unavoidably causes some trial vectors to violate the boundary constraints. In our application, violating the boundary constraints means the source is outside the object, which leads to a failure in objective function evaluation. To keep the boundary constraints strict, we can apply a penalty or use a bounce-back mechanism. The penalty method discards the constraint violated trial vector, while the bounce-back replaces it with a valid one. We prefer the latter boundary satisfaction strategy, because it will perform better sampling near the boundary. The bounce-back is given as follows:

$$u_j = \begin{cases} x_{r_0,j} + \langle 0,1 \rangle \cdot (x_{l,j} - x_{r_0,j}), & u_j < x_{l,j} \\ x_{r_0,j} + \langle 0,1 \rangle \cdot (x_{u,j} - x_{r_0,j}), & u_j > x_{u,j} \\ u_j & \textit{otherwise} \end{cases} \tag{5-7}$$

where u_j is the *j*-th element of the trial vector **U**, $x_{r_0,j}$ is the *j*-th element of the base vector $\mathbf{S}_{r_0}$, $x_{l,j}$ is the lower bound of the *j*-th element of a solution vector, $x_{u,j}$ is the upper bound. The beauty of this simple but powerful operator is that it can adjust the step size of the perturbation without additional computation or input. In the early stage of the

optimization, the vector differences are large because of the wide spread population. As the search proceeds, the candidate solution vectors aggregate to promising areas in the search landscape, so the vector differences become smaller, and the vector difference operator becomes a fine-tuning operator. Such a spontaneous self-adaptation mechanism provides the DE algorithm with a balanced exploration/exploitation and high numerical precision.

DE could use several crossover schemes, such as binomial, exponential, or either-or. We adopt the most commonly used binomial crossover scheme, which is given by

$$\mathbf{s}_j \otimes u_j = \begin{cases} u_j, & \langle 0,1 \rangle \le CR \text{ or } j = j_{rand} \\ \mathbf{s}_j & otherwise \end{cases} \tag{5-8}$$

where $\otimes$ is the crossover operator, *CR* is the crossover rate. Randomly picking an index j_{rand} prevents the duplication of the target vector when a very low crossover rate is applied. The binomial crossover mutates the target vector: with zero crossover rate, only the $j_{rand} - th$ element in the solution vector is mutated; and with ~ 1 crossover rate, the target vector is almost entirely being replaced by the trial vector. The high crossover rate leads to better convergence behavior, but it could expedite the convergence so much that the search converges prematurely. In contrast, a low crossover rate is unlikely to experience stagnation, but the population takes longer to converge. To take advantages of both high and low crossover rates and minimize their shortcomings, we proposed a two-stage crossover scheme for the DE: in stage one, the algorithm operates with a low crossover rate, i.e., CR $\le$ 0.2, for a certain number of generations, then the algorithm switches to a high crossover rate state, i.e., CR $\ge$ 0.8, which speeds up the convergence. The search is then terminated when a majority, i.e., $\ge$ 95% of the population converges to

a single point. The two-stage optimization is especially useful for highly multimodal landscapes, where an over expedited convergence is often a premature one.

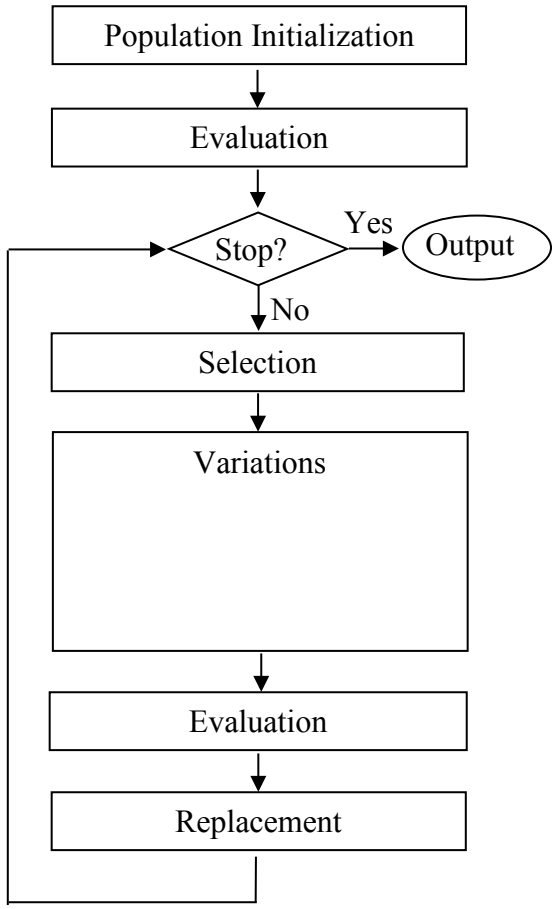

Figure 5-1. *General structure of evolutions algorithms.*

set the number of sources $N \Leftarrow 0$
while $N < N_{MAX}$ or NOT over-represent **do**
  $N \Leftarrow N + 1$
  initialize each candidate solution $X_i = \{\mathbf{x}_1 \dots \mathbf{x}_P\}$
  evaluate each X_i, $i = 1 \dots P$
  while NOT termination condition reached **do**
    repeat
      $\tau \Leftarrow$ permute $\{1, \dots, P\}$
    until $\tau_i \neq i$, $i = 1 \dots P$
    for $i = 1$ to P **do**
      repeat
        random select $r1, r2$ from $\{1, \dots, P\}$
      until $r1 \neq r2 \neq \tau_i \neq i$
      $U \Leftarrow X_{\tau_i} + F \cdot (X_{r1} - X_{r2})$
      $U \Leftarrow X_i \bigotimes U$
      evaluate U
      if $\varepsilon(U) < \varepsilon(X_i)$ **then**
        $X_i \Leftarrow U$
      end if
    end for
  end while
  $X^{opt} \Leftarrow \min_{X_i} \{\varepsilon(X_i)\}$, $i = 1 \dots P$
  for $j = 1$ to N **do**
    for $k = j + 1$ to N **do**
      if $\|\mathbf{x}_j^{opt} - \mathbf{x}_k^{opt}\| \leq$ resolution **then**
        combine sources $\mathbf{x}_j^{opt}$ and $\mathbf{x}_k^{opt}$
        over-represent $\Leftarrow$ TRUE
      end if
    end for
  end for
end while

Algorithm 5-1. *DE-based heuristic solution for the regularized BLT.*

We have assumed that the number of point sources used in the reconstruction is known. In some imaging applications, the number of sources can be estimated directly by biological means; in other cases, this information is unavailable. We present a method to estimate the number of sources from the reconstruction results iteratively. When the assumed number of point sources used in the reconstruction is slightly larger than the

actual number of sources, several point sources will aggregate to represent a single point source, this situation we call “over representation”. Given a desired spatial resolution, we are able to detect the overrepresented source as multiple point sources aggregate within the desired resolution and can be combined to a single source. The iterative process consists of performing a series of reconstructions with an increasing number of point sources; at the end of each reconstruction, if two or more sources are close enough, they are combined into a single source, hence the overrepresentation is detected and the correct number of sources is determined. With this algorithm, the regularized BLT reconstruction only requires a user-determined spatial resolution for the image as additional a priori information. As a summary, the pseudo code of the DE-based reconstruction algorithm is provided in Algorithm 5-1, where ε is the objective function $\left\|\mathbf{s}_j - \mathbf{s}_k\right\|$ is the distance between source *j* and *k*.

Section 5.3. Numerical Studies

Numerical simulation experiments were performed to verify the proposed methodology using an ellipsoidal digital phantom with semi-principal axes of length 15mm, 7mm, and 7mm. The ellipsoid centered at the origin of a Cartesian coordinate system. The digital phantom was discretized into 7421 nodes and 38160 tetrahedra with an average edge length of 1.2 mm. The photon fluence rate on the boundary was generated using Monte Carlo (MC) simulation [51, 80] and the value is recorded at every surface node of the discretized ellipsoid phantom. The optical parameters of the digital phantom were set to $\mu_a = 0.01\left(mm^{-1}\right)$ and $\mu_s' = 1.0\left(mm^{-1}\right)$. We discussed two models of source distribution with two and three point sources, and generated two datasets of boundary measurements

through, respectively, as shown in Figure 5-2. In the two-source case, the sources locations were assigned as (0.0, 5.0, 5.0) and (5.0, 0.0, 5.0) in Cartesian coordinates using millimeter units. In the three-source case, an additional source at (0.0, 0.0, 2.0) was included. All sources had an equal power of 0.314pico-Watt.

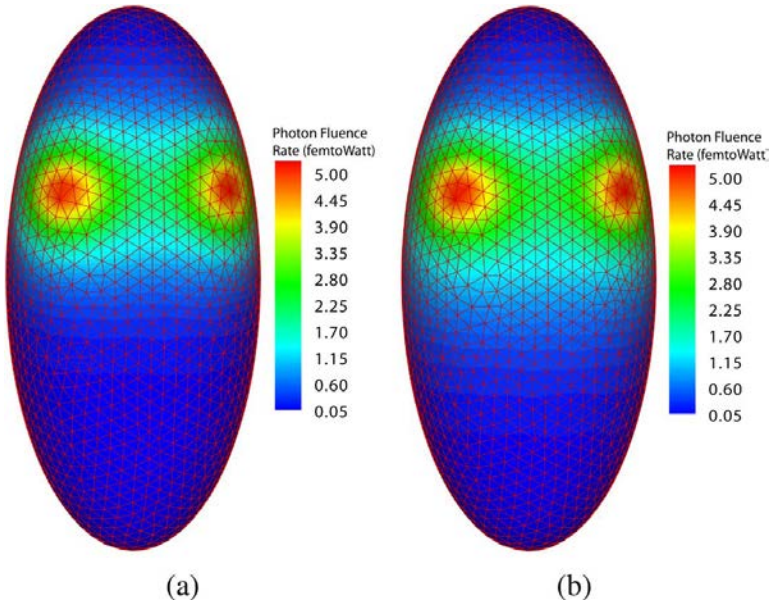

Figure 5-2. *Simulated boundary photon fluence rate from (a) two point sources (b) three point sources.*

Note that not much difference between Figure 5-2(a) and (b) can be directly observed, and the number of sources cannot be confidently estimated through the surface signal. Using the two datasets of boundary measurements, we performed the proposed reconstruction method to recover the number of sources, source locations, and powers from the simulated surface measurement with a desired resolution of 1.6 mm. The reconstructed sources were good agreement to true source distributions, as shown in Figures 5-3(a) and 5-4(a). The extra sources would aggregate around the true source when the number of sources assumed in the reconstruction process was greater than the

actual number. If the separations of aggregated sources were within the desired resolution, they would be combined as a light source. In this way, the number of point sources in both source distribution model was correctly identified, as shown in Figures5-3(b) and 5-4(b). The final reconstruction with the correct number of sources was able to represent the source distribution accurately within the desired resolution.

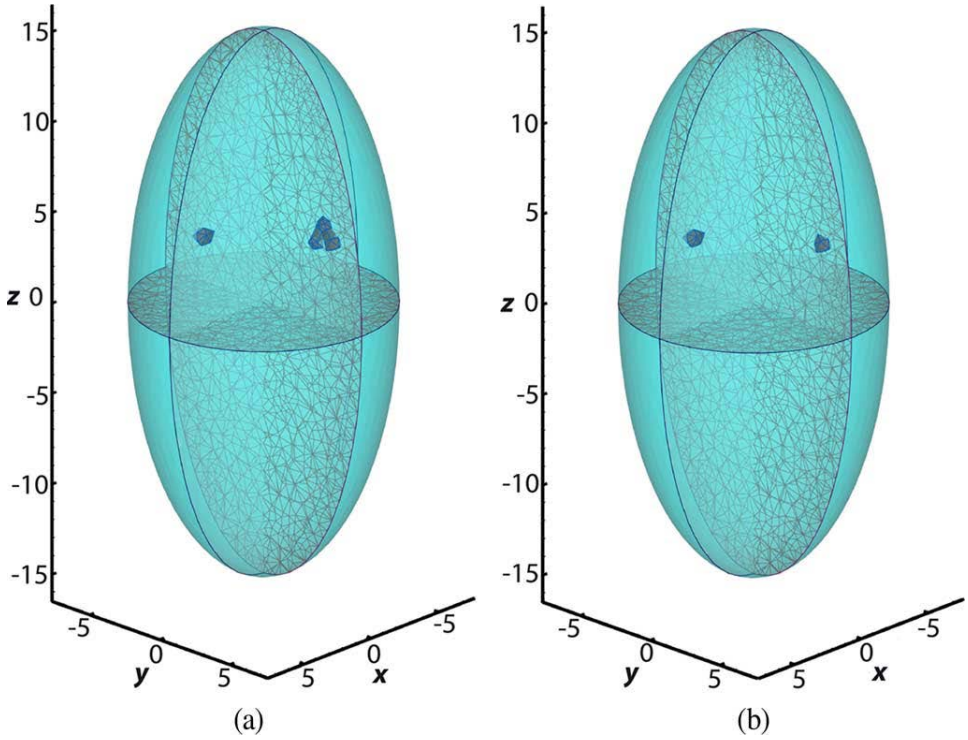

Figure 5-3. *Reconstruction results of two bioluminescence sources. (a) Two extra sources were assumed. (b) Exact number of sources was used*.

The reconstructed point source positions and source powers are listed in Tables 5-1 and 5-2 for the two-source and three-source cases, respectively. The maximum error for source position was 0.6 mm and the maximum relative error for source power was 8%. The reconstruction used a population size of 100, a vector difference scale factor of 0.5, a low crossover rate of 0.2 for the first 100 generations, and a high crossover rate of 0.9

until convergence. The computation time was 30 and 45 seconds on a workstation with a 2.6 GHz Intel Xeon processor for the two-source and three-source cases, respectively.

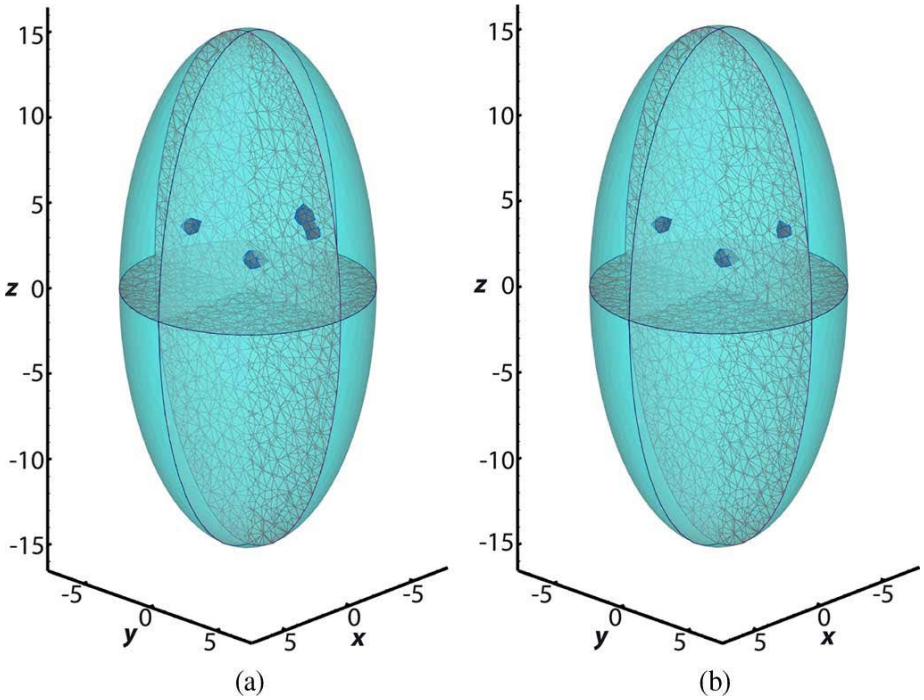

Figure 5-4. *Reconstruction result of three bioluminescence sources. (a) One extra source was assumed. (b) Exact number of sources was used.*

Table 5-1. Reconstruction Result for Two Point Sources

Source #	X (mm)	Y (mm)	Z (mm)	Power (picoWatt)
1	0.098	5.029	4.584	0.336
2	4.5	0.159	4.925	0.293

Table 5-2. Reconstruction Result for Three Point Sources

Source #	X (mm)	Y (mm)	Z (mm)	Power (picoWatt)
1	0.098	5.029	4.584	0.329
2	4.5	0.159	4.925	0.301
3	0.074	0.552	1.785	0.289

Aside from the reconstruction accuracy, we tested the reconstruction robustness against inaccurate optical parameters. In most BLT applications, the optical parameters of the biological tissues used in the reconstruction have various degree of inaccuracy. Inaccurate tissue optical properties could affect the reconstruction accuracy significantly [81, 82]. We investigated the impact of optical parameter variation on the proposed BLT model and DE-based reconstruction method by adding ±10% perturbation to absorption and reduced scattering coefficients in a MC simulation. The simulations were performed on the same ellipsoidal digital phantom with two point sources at (0.0, 5.0, 5.0) and (5.0, 0.0, 5.0), and used similar settings as the previous analysis. The actual absorption coefficient and reduced scattering are $\mu_a = 0.01\, mm^{-1}$ and $\mu_s' = 1.0\, mm^{-1}$. The results (see Tables 5-3 and 5-4) show that the proposed reconstruction method is robust against optical parameter perturbation, especially for source position.

Table 5-3. Effects of absorption coefficient variation on reconstruction results

	$\mu_a = 0.009\, mm^{-1}$	$\mu_a = 0.011\, mm^{-1}$
Source 1 position error (mm)	0.82	0.43
Source 1 power error (%)	17%	13%
Source 2 position error (mm)	0.53	0.53
Source 2 power error (%)	15%	11%

Table 5-4. Effects of reduced scattering coefficient variation on reconstruction results

	$\mu_s' = 0.9\, mm^{-1}$	$\mu_s' = 1.1\, mm^{-1}$
Source 1 position error (mm)	1.42	0.43
Source 1 power error (%)	23%	19%
Source 2 position error (mm)	0.53	0.53
Source 2 power error (%)	19%	18%

Based on the model with three-source distribution, optical parameters and boundary data same to above description, we further implement the reconstruction of light sources using the popular regularization optimization-based reconstruction method [16-18]. As a result, the reconstructed light source distribution has a big difference to true source distribution, as shown in Figure 5-5. The reason is the ill-posedness of the conventional inverse model, which commonly lead to nonunique solutions and aberrant reconstruction in the presence of measurement noise and optical parameter mismatches. Although regularization technique may improve the reconstruction, the solution sensitively depends on the regularization parameters, which small variation of regularization parameter would lead to a big difference of the reconstructed light source distribution. Moreover, the number of light sources inside object is not constrained in the conventional reconstruction method, which often reconstructs multiple light sources with low powers instead of a true light source, resulting in a total different light source distribution.

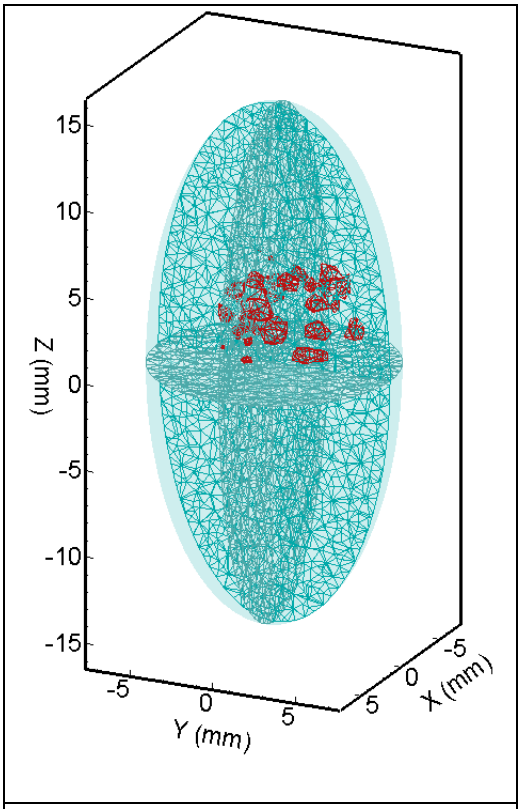

Figure 5-5. *Reconstruction result of three bioluminescence sources using conventional regularization method.*

Section 5.4. Experiments and Reconstruction Results

We apply the regularized reconstruction method for a phantom study. The phantom experiment was performed on a mouse-shaped phantom with two embedded LED

sources, as shown in Figure 5-6. The positions of the LEDs were revealed by computed tomography (CT) scan of the phantom, shown in Figure 5-7.

We performed the experiment using both LEDs as light sources. The LED near the neck had an intensity of 1.11×10^{11} photons/s and the intensity of the LED at the abdomen was 1.25×10^{11} photons/s. The surface photon fluence was measured using Xenogen's IVIS 100 series imaging system. A filter of 515–575 nm was used to limit the spectrum of the signal, and the corresponding optical parameters of the phantom were $\mu_a = 0.091\, mm^{-1}$ and $\mu_s' = 1.88\, mm^{-1}$. In contrast to the popular four-view configuration for BLT, we only captured partial measurements from dorsal and ventral views to demonstrate the robustness of the reconstruction. The surface measurements were normalized. A geometrical model of the phantom was constructed from the CT scan images using Amira 4.0 (Visage Imaging, Inc.). The geometrical model was discretized into 14844 nodes and 75107 tetrahedra. The partial surface measurements were mapped to the corresponding boundary nodes of the model, as shown in Figure 5-8.

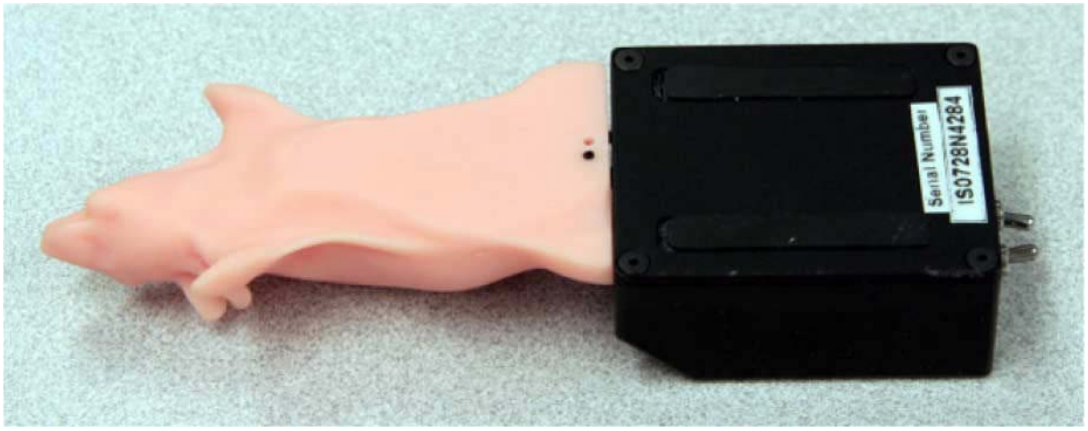

Figure 5-6. *Mouse-shaped phantom from Caliper Life Sciences.*

Using the same optimization parameter configuration previously presented, the reconstruction took one minute and ten seconds on the same Intel Xeon workstation. The reconstructed source locations are shown in Fig. 5-9. The difference between the reconstructed locations and the LED positions measured on the CT scan images were less than 2 mm, and the reconstructed source strength ratio was 1.52:1 for the LED in the abdomen region versus the one near the neck.

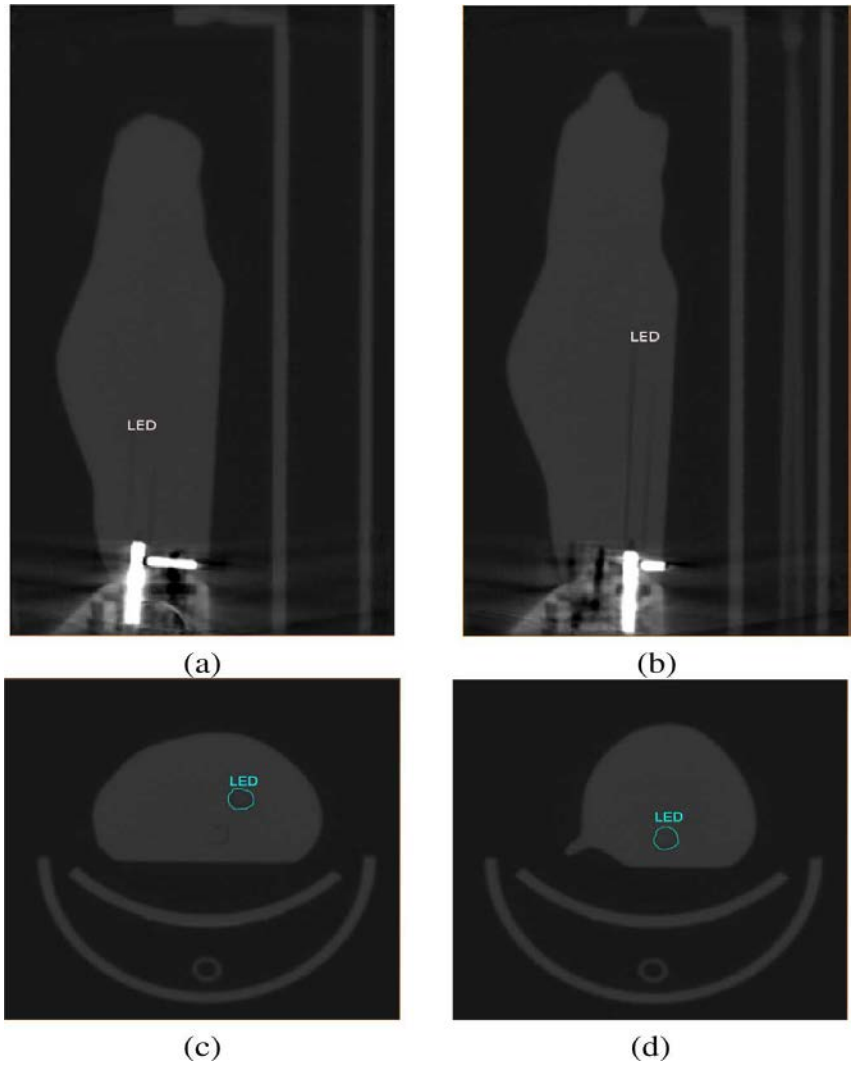

Figure 5-7.*CT scan reveals LEDs' positions in the phantom. (a) sagittal view of LED 1; (b) sagittal view of LED 2; (c) axial view of LED 1; (d) axial view of LED 2.*

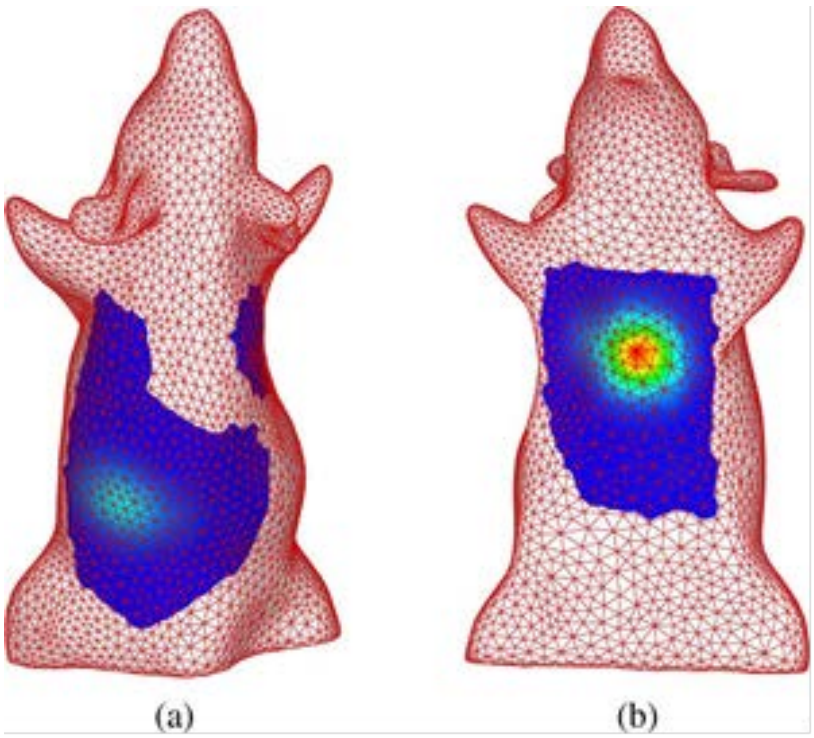

Figure 5-8. *Partial surface photon fluence rate. (a) dorsal view; (b) ventral view.*

Finally, we applied the proposed method to detect tumors labeled with firefly luciferase reporters in a mouse study. Tumors were induced by injecting the 22Rv1-luciferase human prostate cancer cell line intracardially into severe combined immunodeficiency (SCID) mice. After a few weeks, a cancer-bearing mouse was injected with D-luciferin at a dose of 100μl per 10g body weight. The surface photon emission of the bioluminescent reporters, as shown in Figure 5-10, was captured by a highly sensitive liquid nitrogen-cooled CCD camera (Figure. 5-11) using four views, as in Figure 5-12. The mouse abdominal section was scanned using micro-CT and a finite-element model that described the optical property heterogeneity was constructed from the CT image volume using Amira 4.1 (Visage Imaging, Andover, MA), as shown in Figure 5-13(a).

The model consisted of 15971 nodes and 87513 tetrahedral elements. The optical parameters of each organ are listed in Table 4-5 [61].

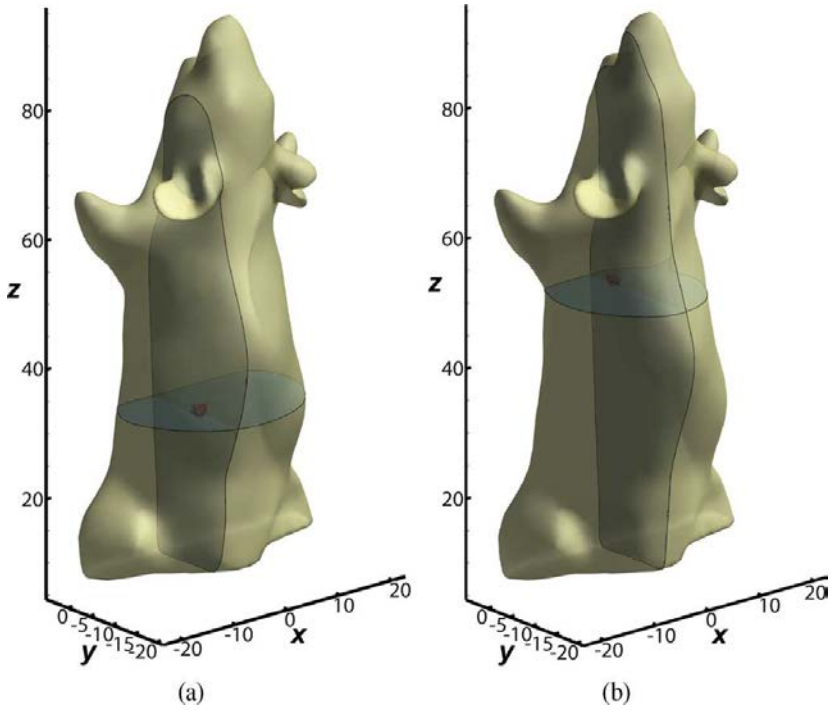

Figure 5-9. *Reconstruction results of LED sources. (a) Reconstructed location of LED1. (b) Reconstructed locations of LED2.*

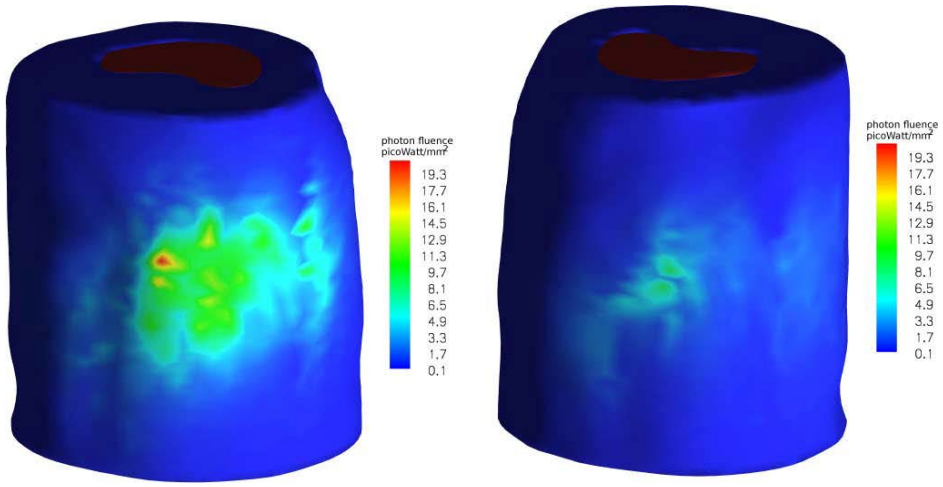

Figure 5-10. Surface photon fluence mapped to mouse geometrical model. (a) dorsal view. (b) ventral view.

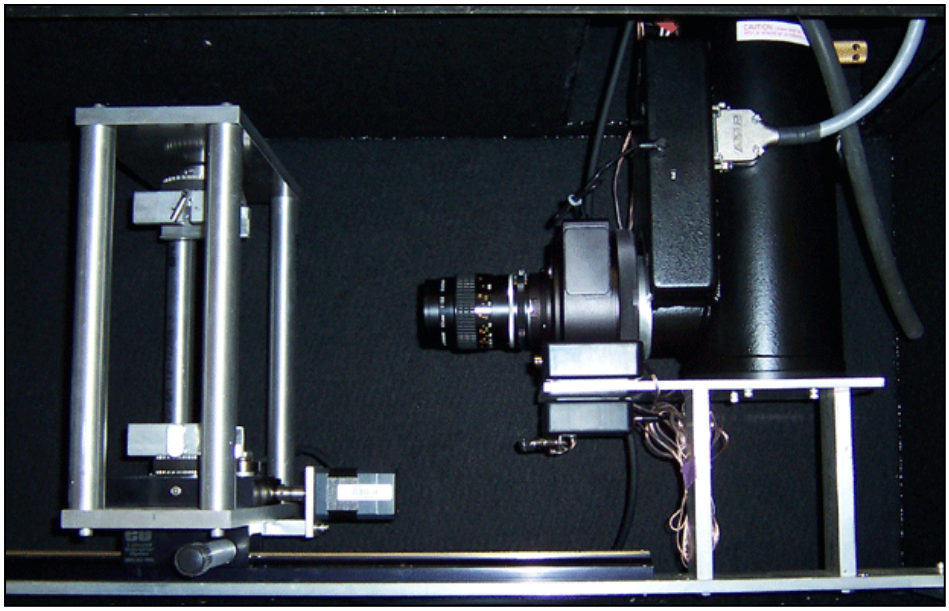

Figure 5-11*. Bioluminescence tomography system with liquid nitrogen-cooled CCD camera.*

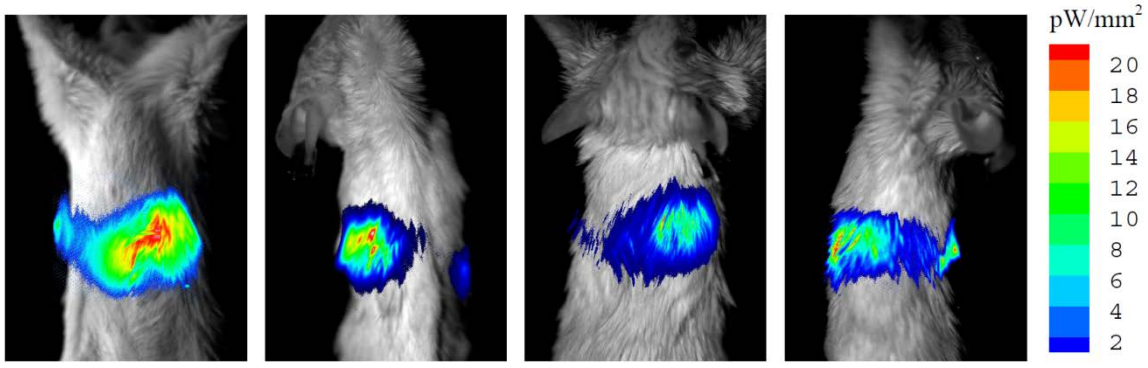

Figure 5-12. *Four bioluminescence views. (a) anterior-posterior view (b) right lateral view (c) posterior-anterior view and (d) left lateral view.*

We set the population size to 150. The reconstruction took one minute and forty seconds on an Intel Xeon workstation. Two tumors, located on top of the kidneys were found; the tumor locations are presented in Fig. 5-13(b). The reconstructed source powers

are 14.4 nanoWatt for the bigger tumor and 8.6 nanoWatt for the small tumor. For verification, the mouse was dissected to locate the tumors (Fig. 5-13(c)): one tumor was found on each adrenal gland with volumes of 468 mm^3 on the right and 275 mm^3 on the left, which had good agreement with the reconstruction. The reconstruction using the proposed method is also consistent with previously published reconstruction results on the same dataset.

Table 5-5. Approximated Optical Parameters for Mouse Organs

Organs	$\mu_a \left(mm^{-1}\right)$	$\mu_s' \left(mm^{-1}\right)$
Muscle	0.23	1.00
Liver	0.45	2.00
Stomach	0.21	1.70
Kidney	0.12	1.20

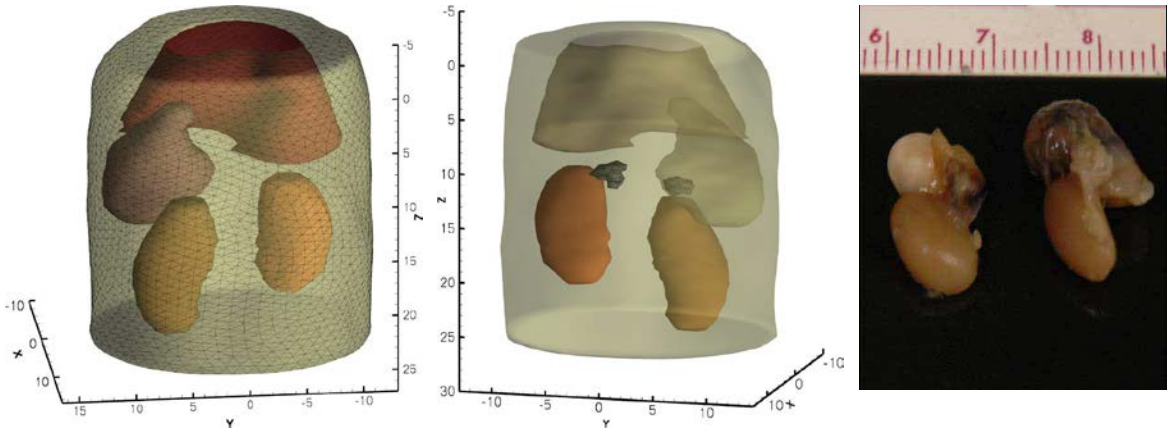

(a) (b) (c)

Figure 5-13. *Reconstruction of adrenal gland tumors. (a) Finite-element model of the abdominal section of the mouse, (b) Reconstructed adrenal gland tumors vs. histological verification (c).*

In summary, we proposed a regularized inverse source model that incorporates the number of sources as a constraint and devised a scheme to determine the number of sources automatically. The regularized inverse source model significantly reduced the number of variables in the optimization procedure, and more importantly, produced a unique solution. Furthermore, we adapted the DE method to solve this optimization in a two stage variation for efficient source reconstruction. The DE integrates the number of sources constraint directly into its versatile solution vector encoding scheme. DE also has the ability to locate the global optimum regardless of the initial values, and exhibits a fast and reliable convergence behavior. Using numerical studies, we demonstrated that the proposed method is able to accurately localize and quantify light source distribution from noisy measurements and inaccurate optical parameters. The phantom study further demonstrated the robustness of the proposed method by locating the LED sources using measurements that only covered part of the surface. This result suggests that the proposed reconstruction method could reduce the imaging time and facilitate the hardware design. The in vivo study presented a practical example of the effectiveness of the method, and the result showed a good agreement with the histological verification along with consistency with the previously published results. However, there are several major limitations to the proposed method. First, the optimization problem has a dimension that equals to four times the number of sources. The population size and generation of the optimization problem will increase rapidly as the dimensionality increases; therefore, the DE optimization method is not suitable for the source distributions that need to be approximated by too many point sources. Second, although the regularized model is well applied to small isolated source reconstruction, the regularized model may not work well

on distributed sources. The application of the proposed model to the distributed source is worth a systematic study in the future. Third, the iterative method for estimating the number of point sources needs to solve the reconstruction problem several times, and only one of the many reconstructions is used as the final result; therefore, when the number of sources cannot be determined from a priori knowledge, the computational efficiency will be greatly compromised. We also emphasize that our regularized BLT model is converted to an optimization with complex constraints. The resulting optimization problem cannot be adequately solved by a gradient-based optimization method; therefore, a fair comparison in performance between the DE-based method and the gradient-based method cannot be easily implemented.

Chapter 6. Monte Carlo Fluorescence Microtomography

Fluorescence molecular imaging is a very popular method to study biological molecules, pathways and events in living cells and tissues. With its sensitivity, specificity, non-invasiveness and cost-effectiveness, fluorescence molecular imaging is widely applied in preclinical and clinical applications. An important application of optical imaging for regenerative medicine and tissue engineering is to monitor cell growth and distribution in the scaffold. Tissue regeneration involves extensive remodeling of cells and scaffolds. Cells are labeled with GFP and mKate fluorophores and seeded on the scaffolds. Cells are visualized in the blue, green and red channels with a fluorescent microscope. From the measured fluorescence data, we further resolve the labeled cell distributions in 3D in order to monitor cell proliferation and migration in a bioengineered blood vessel using optical tomography. The visualization of biological processes in living systems has the main expectation in localization and quantification of molecular changes associated with a disease at an early stage rather than later when morphological changes have occurred. Fluorescence molecular imaging is used to visualize the development of bioengineered blood vessels in bioreactors and after implantation into living animals in real-time for the applications of regenerative medicine.

The imaging limit of conventional microscopy can be derived from the mean free path (MFP) of a photon. The MFP describes the average distance that a photon travels between two consecutive scattering events. The MFP is of the order of 100 μm in tissue, which means that the bulk of photons propagating through a 100-μm tissue slice will experience at least one scattering event, resulting in image blur. Photon scattering

degrades this ability at increasing depth, and fundamentally limits the penetration capacity of microscopic imaging. Confocal and multiphoton microscopy have been developed to image specimens thicker than 10–20 μm, and have revolutionized biological discovery by allowing the noninvasive study of life processes in unperturbed environments. The increasing need to study biological processes *in vivo* has driven the development of photonic methods that can be used to image well beyond the penetration limits of conventional microscopy. Because of the intense light scattering it becomes difficult to image fluorescence probe distributions with thicker tissue samples using current fluorescence microscopy techniques. After propagating over a few hundred micrometers, fluorescence light would become highly diffusive. The state-of-the-art microscope operates only at depths less than one transport mean free path length in tissue. With the intense scattering signal, it becomes difficult to image a fluorescence probe distribution within a thick biological sample using the current fluorescence microscopy.

In this chapter, we present a fluorescence tomographic method to reconstruct an optical molecular probe distribution using a standard fluorescence microscope on a thick biological sample [83]. The light propagation through the biological tissue is a complicated process that involves both absorption and scattering. The photon propagation model governs the interaction between light and tissues, and is essential for tomographic imaging with visible and near-IR light. The popular diffusion approximation model (DA) is fairly accurate and efficient in the cases of highly scattering and weakly absorption in a large tissue sample. However, the DA model suffers from a substantial discrepancy near either sources or boundaries, which happens to be the case of microscopic imaging [55].

As introduced in Section 3.5, Monte Carlo simulation (MC) is a statistical technique that accurately traces photon paths in the biological environment. The MC method is based on randomly constructing a set of trajectories of photons propagation in tissues while the step size and direction of each trajectory depends on the absorption and scattering properties of tissues. The MC method can give an accurate estimation for light propagation. However, the MC method takes long computation time. MC simulation could be sped up by the parallel computation, such as CPU clustered supercomputers. However, traditionally supercomputers are neither readily available nor accessible to most researchers and clinical users due to the prohibitively high cost of facility deployment and maintenance. Recently, the massive parallel approach using general-purpose graphic processing units (GPGPU) has been adopted to speed up the MC simulation. GPU is well suitable for the problems that can be parallel executed due to its special architecture. Alerstam*et al.* showed that GPU-based acceleration could be applied in the MC simulation to obtain a massive speedup over the traditional CPU implementation[84]. We implemented a GPU-based Monte Carlo simulator on a multi-GPU system with the CUDA platform [85, 86]. Using four NVidia Tesla C1050 GPUs, we are able to archive a speedup of over 800 times compared to the same implementation on a single Intel Xeon CPU core, enabling the Monte Carlo method to be used in the inverse process.

Section 6.1. Inverse Monte Carlo Reconstruction

Using the GPU-based Monte Carlo simulation, we developed a Monte Carlo algorithm for fluorescence tomography. Usually, microscopic imaging focuses on a region of interest (ROI) in the biological sample and acquires surface fluorescence scattering

signals emitted from optical molecular probes in the ROI. The ROI volume can be discretized into finite volumetric elements. Based on Eq. (4-8), the acquired photon fluence rate data on the surface of the ROI is a linear combination of fluorescence source intensities,

$$\mathbf{\Phi} = \mathbf{A} \cdot \mathbf{S} \tag{6-1}$$

where Φ is a vector of the photon fluence rate measured at each pixel, **S** a vector of fluorescence source intensities, and **A** the discrete Green function. A column vector of **A** is constructed from the photon fluence rate at each pixel computed from the GPU-based Monte Carlo simulator assuming that each potential elemental fluorescence source has unit intensity.

In practice, the measurable quantity Φ in Eq. (6-1) can only be collected on a partial external surface of an object, either upside or downside of a biological sample, while the fluorescence sources are distributed in a 3D domain. Clearly, the source reconstruction is an ill-conditioned problem, which often produces false solutions due to the existence of multiple solutions and the presence of measurement noise. Regularization is often used to stabilize the reconstruction. With the use of regularization, such as Tikhonov regularization, feasible region constraint, and compressive sensing-based l_1-norm regularization, fluorescence tomography shows improvements but the ill-posedness of the problem remains.

To find a stable solution, here we introduce a well-posed model to regularize the inverse source problem: given the prior optical parameters of the sample including the absorption coefficient μ_a, scattering coefficient μ_s, and anisotropic factor g, then the positions and powers of luminescent sources can be uniquely determined from the

measurable diffused light signal on the boundary of the ROI under the assumption that the number of isolated luminescent sources *n* is known in the ROI. Based on this concept, Eq. (6-1) can be converted to an optimization problem:

$$\begin{cases} \min\limits_{\mathbf{S}} \left\| \mathbf{AS} - \mathbf{\Phi} \right\| \\ s.t. \quad s_{i_k} > 0, \quad k = 1, 2, \cdots, n \\ \qquad s_j = 0, \quad j \notin \{i_1, i_2, \cdots, i_n\} \end{cases} \tag{6-2}$$

where the vector **S** only includes *n* positive nonzero values $\{s_{i_1}, s_{i_2}, \cdots, s_{i_n}\}$, which represents the power of the fluorescence sources, and its index $\{i_1, i_2, \cdots, i_n\}$ correspond to the source positions. The new reconstruction model based on Eq. (6-2) has a unique solution, and can effectively overcome the ill-posedness of fluorescence tomography.

Eq. (6-2) is an optimization problem subject to complex constrains, which is NP-hard, and cannot be solved efficiently using a commonly adopted gradient-based optimization method. In the work, we developed a differential evolution (DE)-based heuristic reconstruction algorithm to solve the optimization problem[20, 76]. DE is based on a spontaneous self-adaptive vector difference operator, and displayed a superior converging behavior with a high precision. Experience with numerous benchmark and real-life problems suggests that the DE often has a fast and reliable converging behavior with a relatively small population size [87]. Each candidate solution in DE is a weighted combination of the columns in **A**. Due to the rapid convergence of DE, the optimizer can delineate the feasible region of the fluorescence sources in a few generations (i.e., iterations), and many of the columns in the discrete Green function **A** are never used. Taking advantage of this observation, we replace the full Green function construction with an on-the-fly evaluation scheme: whenever a column in **A** is needed in a candidate

solution, and has not been evaluated, that column will be computed by performing the Monte Carlo simulation. Comparing to the full Green function evaluation, the on-the-fly scheme saves about 40-70% of Monte Carlo runs, which further speeds up the reconstruction process.

The constraint on the number of light sources, however, cannot be always obtained from in advance. We can heuristically determine the number of light sources by gradually increasing the number of sources and solve the optimization problem in Eq. (4.2). For each reconstructed source distribution, if two or more sources are so close that they cannot be isolated within a user-provided spatial resolution, they are combined into a single source. After the source combination, the source distribution is equivalent to a previous reconstructed counterpart with a smaller number of sources. Such a number can always be iteratively and heuristically determined to interpret measured data effectively and efficiently.

Section 6.2. Experimental Studies

We investigated the accuracy and robustness of the proposed fluorescence microtomography approach in experiments on biomimetic tissue scaffolds. Three poly (D, L-lactide) (PDLA) scaffolds were fabricated using an electrospinning technique with thicknesses of 0.65, 0.8, and 1.4 mm, respectively. The optical properties were measured using a spectrophotometer (Varian Cary 5000 UV-Vis-

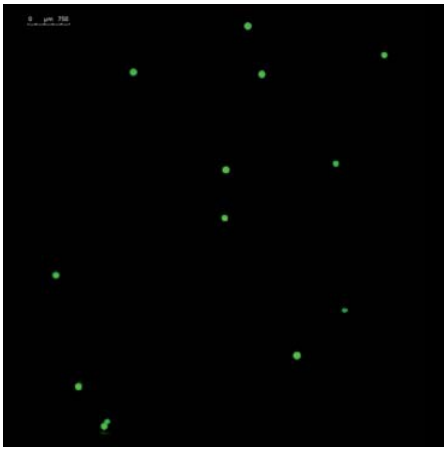

Figure 6-1. Microbead distribution in the scaffold.

NIR, GMI, Inc.). The absorption coefficient is approximately 0.01(mm^{-1}), the scattering coefficient 15.0 (mm^{-1}), and the anisotropic factor 0.9. Fluorescence microbeads of 90 micron diameter (Spherotech Inc.) were laminated and pressed onto each scaffold sample to mimic green fluorescence labeled cells. The actual microbead distribution was captured under a fluorescence microscope, as shown in Figure 6-1, and serves as the control image. The scaffold was illuminated using a uniform field of blue laser light (λ = 473nm) to excite the microbeads, and the emission signal captured using an EMCCD camera with a 1x long working distance lens (Mitutoyo, M Plan 1x), creating a field of view of 8.192mm×8.192mm same as the size of the EMCCD sensor, as shown in Figure 6-2. From each set of captured emission signals, we reconstructed the microbead distribution using the proposed reconstruction method, as shown in Figure 6-3. The results show no significant difference in localization accuracy over all the scaffold thicknesses. Fig. 6-3(b), (e) and (h) present maximum position errors of ~250 micron, ~275 micron and ~500 micron respectively. These reconstruction errors were relative to the size of ROI, and induced from the measurement noise rather than the ill-posedness of

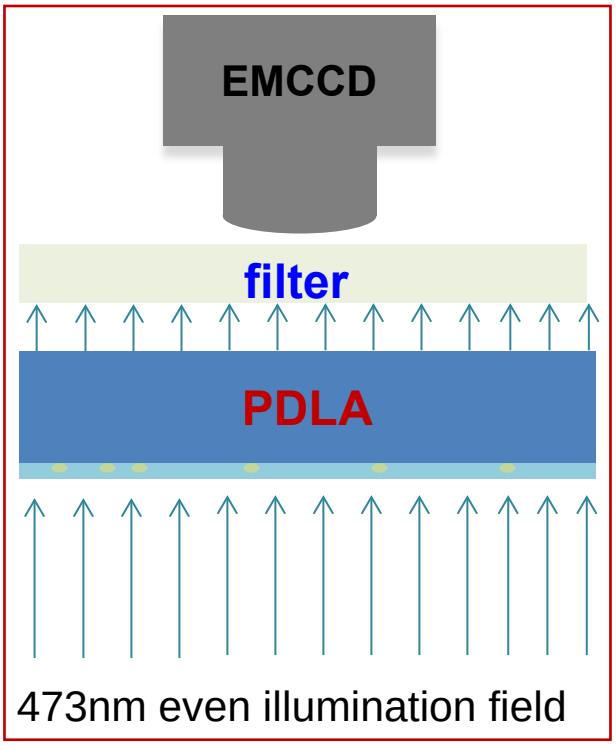

Figure 6-2. Schematic diagram of the microbead imaging experiment.

the reconstruction. This claim was confirmed in our numerical simulation where a reduced measurement noise was correlated to improved location accuracy.

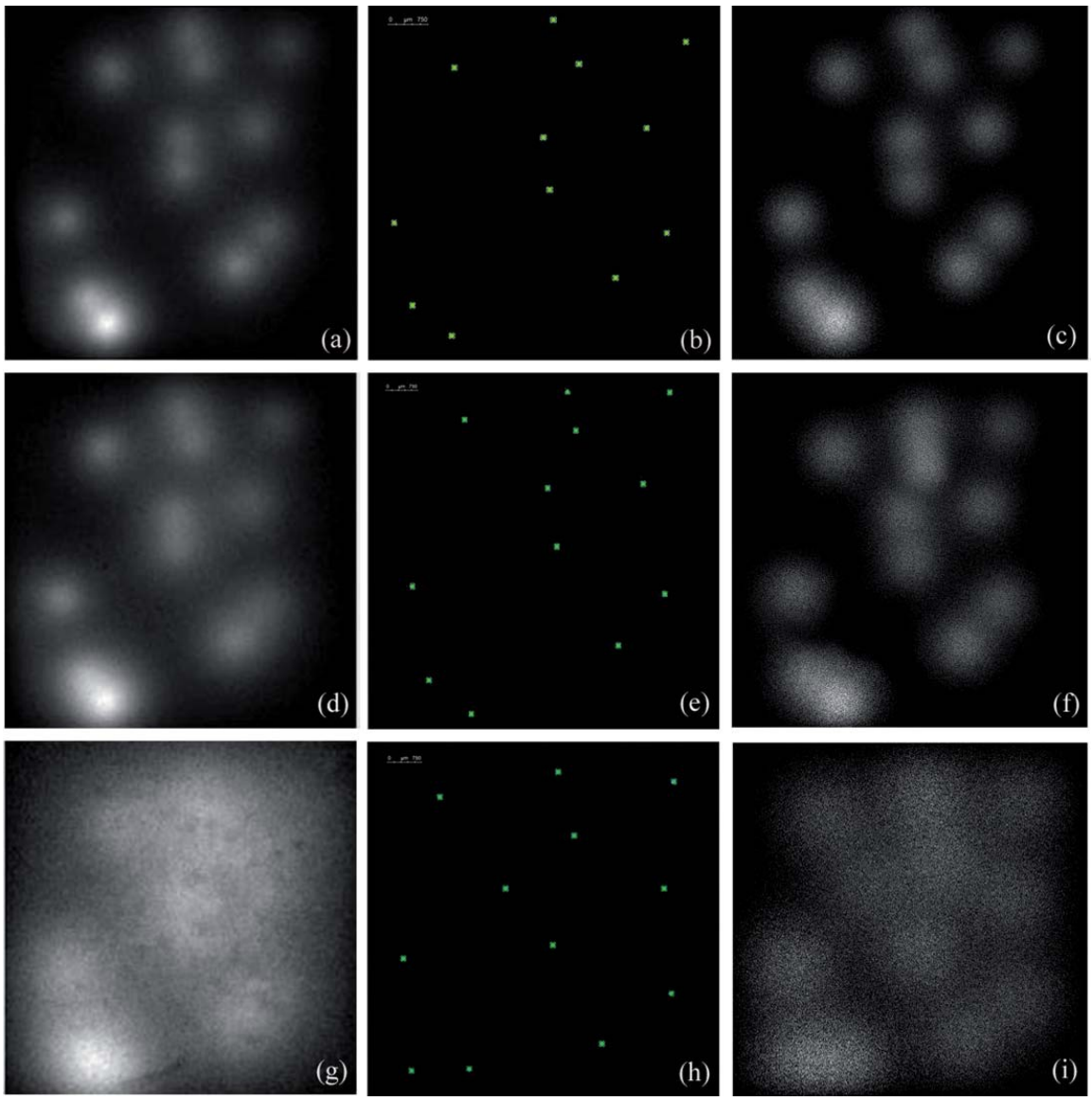

Figure 6-3. *Scaffold experiment results. (a) An microbead fluorescence emission image from a 0.65 mm thick scaffold; (b) a reconstructed microbead distribution from (a); (c) the projected fluorescence emission image from (b); (d) a microbead fluorescence emission image from a 0.8 mm thick scaffold; (e) the reconstructed microbeaddistribution from (d); (f) the projected fluorescence emission image from (e); (g) a microbead fluorescence emission image from a 1.4 mm thick scaffold; (h) the reconstructed microbead distribution from (g); and (i) the projected fluorescence emission image from (h).*

We also performed the reconstruction of microbead distribution from same dataset described above for the sample with a 0.65 mm thick scaffold using popular regularized optimization method and conventional inverse source model. As a result, the reconstructed microbead distribution has a significant difference to the true distribution, as shown in Figure 6-4. The conventional inverse source model is ill-posed for reconstruction of multiple sources, and often produces false solutions due to the existence of multiple solutions and the presence of measurement noise.

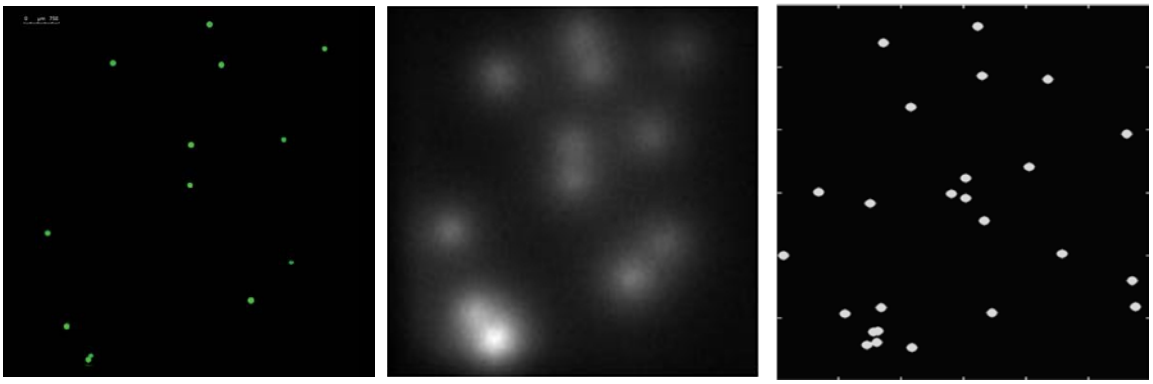

Figure 6-4. *Reconstructed microbead distribution (right) from fluorescence emission image of a 0.65 mm thick scaffold (center) using conventional inverse source model; the true distribution is on the left.*

In summary, we have developed a novel fluorescence microtomography approach to reconstruct fluorescence reporters in thick biological samples. This tomographic imaging method is based on a well-posed inverse model we have established, and has a unique and stable solution. Our experiments have demonstrated that the proposed fluorescence microtomographic method is able to localize and quantify an optical molecular probe distribution accurately, up to a spatial resolution of several hundred microns in relatively thick and highly opaque samples. Using higher powered microscope, we expect further improvement in spatial resolution.

Chapter 7. Conclusion

Section 7.1 Main Contributions

Optical molecular imaging is to monitor physiological and pathological activities in small-animal models at the cellular and molecular levels non-invasively. With its high sensitivity and low cost, the optical molecular imaging has significant applications in pre-clinical researches. Optical molecular tomography is to localize and quantify optical molecular probe distribution in 3D from the measured optical signal on mouse external surface. The researches mainly focus on photon propagation modeling in biological tissues and reconstruction algorithms for optical molecular tomography. The main contributions are summarized as follows.

The optical molecular tomographic imaging relies on the optical parameters of tissues, which would produce a significant effect on the reconstruction image of molecular probes [82]. We have proposed a method to estimate the optical parameters for the phase-approximation (PA) model. Specifically, we have designed an iterative algorithm to take advantage of both the global search ability of the differential evolution algorithm and the efficiency of the conjugate gradient method. We demonstrated the feasibility and merits of the proposed method in both numerical simulation and phantom experiments. The proposed optical property characterization method, along with the PA model would improve the accuracy of optical molecular tomographic imaging.

The reconstruction of inverse source problem is ill-posed, commonly leading to non-unique solutions and aberrant reconstruction in the presence of measurement noise and optical parameter mismatch. Existing works were mainly based on an ill-posed inverse source model, and applied the regularization method to improve the

reconstruction. However, the reconstructed result is very sensitive to regularization parameter selection; a small variation of regularization parameters would lead to a big difference of the reconstructed light source distribution. Moreover, the reconstruction of multiple light sources in an object would face increased challenges. We published the first paper on multispectral bioluminescence tomography (BLT). The multispectral BLT approach improves the accuracy and stability of the BLT reconstruction. Furthermore, we presented a novel inverse source model for optical molecular tomography with the knowledge of the number of light sources. This new model is well-posed and has a unique and stable solution. Based on this model, we developed a differential evolution-based reconstruction algorithm to determine the source location and strength accurately and reliably. The numerical and phantom experiments, and mouse studies have verified the proposed approach can achieve accurate and stability solution. To enhance the spatial resolution of fluorescence tomography into micron scale, we proposed the first optical-based fluorescence microtomography to image cells in a tissue scaffold based on Monte Carlo simulation [83]. We demonstrated the efficiency and accuracy of the inverse Monte Carlo method on a massive parallel processing architecture.

Section 7.2. Software Developments

Scientific research is only meaningful if the results are reproducible. However, many published research results are not reproducible and independently verifiable. The lack of reproducibility severely undermines the practical impact and even the authenticity of the research work. The major problem is that the traditional scientific publication is limited to the paper medium, which prohibits a complete documentation of the research work. Computer program source files are often unavailable. Even with the authors' source

code, failure to replicate reported results often caused by the lacks of guidance to compile and execute the program. Availability and compatibility of operating system, compiler tool chain, and libraries can further hinder the portability of source code distribution. Such difficulties often dismiss the effort to reproduce, verify and reuse other researchers' product. In our research, we produced several computer programs to implement the reconstruction algorithms. The programs are written in C++, and Intel C++ compiler and Intel Math Kernel library are used. The programs are compiled and executed under Linux platform. Programs use simple command-line interface.

Typical method of reproducible research involves heavy documentation and programming guideline. In addition to proper documentation and abiding the guidelines, we proposed software as a service (SaaS) solution to promote reproducible scientific computation. Instead of distributing the source code and let end users to deploy the program locally; we directly deploy our programs on internet cloud servers. Amazon EC2 provides powerful computation oriented instances that fit our intense computation needs. A web interface to our program will be programmed using JSP and Servlet. Researchers who need to execute our programs can do so via web interface in a browser. Amazon S2 service can provide adequate storage of the user uploaded and result data. The SaaS solution will provide a quick and easy way to reproduce results, and potentially increase the impact of our work.

Section 7.3. Future Topics

Nanoparticles are particularly useful as imaging probes because of their unique physicochemical properties and their apparent lack of overt toxicity. The surface area to volume ratio increases as spherical particles decrease in diameter. A high ratio allows for

greater surface functionality, which can be used to tune particles for tissue or cell targeting in vivo. A typical nanoparticle with a diameter of 5–10 nm is similar in size to human albumin and smaller than an immunoglobulin protein. The size of the nanoparticles can result in wider distribution *in vivo* because they are less hindered by biological barriers than larger particles of the same chemical composition. Both the size and surface properties of nanoparticles are important for their interaction with biological systems and their distribution in the circulation. These nanoparticles may passively target tissues or cell types in vivo, or they may be modified with targeting moieties to actively target diseased cells for cancer targeted imaging and therapy.

Typical carbon nano materials, like carbon nanotubes and graphene, have many interesting physical and chemical properties that are potentially useful in biological and biomedical applications [88, 89]. Well-functionalized carbon nanotubes stable in physiological environments have been shown to be nontoxic to cells in vitro and in vivo to mice. Carbon nanotubes have been widely used as drug delivery vehicles for in vitro drug and gene delivery as well as for vivo cancer treatment [90]. In addition, the intrinsic optical properties of single-walled carbon nanotubes (SWNTs), including resonance Raman scattering, near-infrared (NIR) photoluminescence, and NIR optical absorption, can be utilized in biomedical imaging and phototherapy applications.

Recently, biomedical applications of grapheme at the cellular level have been explored. Nanographene sheet (NGS) functionalized with polyethylene glycol (PEG) exhibits high solubility and stability in physiological solutions and has been used for in vitro drug delivery and imaging. By the studies for behaviors of PEGylated NGS in mice by in vivo fluorescence imaging, one observed surprisingly high tumor accumulation of

NGS in a few different xenograft tumor models, likely owing to the enhanced permeability and retention (EPR) effect of cancerous tumors. Using the strong NIR optical absorption ability of NGS for in vivo photothermal therapy of cancer and achieved highly efficient tumor destruction by intravenous NGS injection followed by low power NIR laser irradiation. Highly efficient tumor passive targeting of NGS has been observed in several different tumor models without utilizing any targeting ligands, such as antibodies. Many important applications, observing the NGS targeting, quantifying the NGS accumulation around tumors and the NGS concentration for *in vivo* photothermal therapy of cancer, can be achieved using fluorescence tomographic imaging. Novel contrast agents provide outstanding opportunities to visualize and analyze specific biological targets, signal pathways, and therapeutic responses [91, 92].

The nanophosphors emit near-infrared (NIR) luminescence light upon x-ray excitation [93]. As optical probes, these nanophosphors potentially allow sensitive and specific high-resolution imaging *in vivo*[94]. Using the nanophosphors, x-ray luminescence computed tomography (XLCT) was recently proposed as a new molecular imaging modality [95]. The experiments demonstrated that XLCT could image the cross-sectional distribution of nanophosphors [96]. XLCT has several advantages comparing to other optical molecular imaging modalities. First, the anatomy and the nanophosphors can be imaged in a single scan. Second, the use of x-ray excitation eliminates the autofluorescence in optical fluorescence imaging. Third, the straight line propagation of x-rays in a biological object means a localized and deep probing capability, promising to improve the spatial resolution significantly [95]. Through selective excitation with a pencil x-ray beam, XLCT can perform *in vivo* tomographic imaging on a region of

interest (ROI) to reduce radiation dose and shorten experimental time. This selective excitation mechanism is similar to x-ray fluorescence computed tomography (XFCT), which is used to map elements inside samples. XLCT currently works in a pencil beam scanning mode and need long scanning time. Fan-beam scanning modes can improve the imaging efficiency, and can accurately localize and reliably quantify the nanophosphor distribution in the tissue from the surface NIR measurements.

REFERENCES

1. Weissleder R, Pittet MJ: **Imaging in the era of molecular oncology**. *Nature* 2008, **452**(7187):580-589.
2. Weissleder R, Tung CH, Mahmood U, Bogdanov A: **In vivo imaging of tumors with protease-activated near-infrared fluorescent probes**. *Nat Biotechnol* 1999, **17**:375-378.
3. Weissleder R: **Molecular Imaging in Cancer**. *Science* 2006, **312**:1168-1171.
4. Ntziachristos V, Ripoll J, Wang LHV, Weissleder R: **Looking and listening to light: the evolution of whole-body photonic imaging**. *Nature Biotechnology* 2005, **23**(3):313-320.
5. Contag CH, Bachmann MH: **Advances in vivo bioluminescence imaging of gene expression**. *Annual Review of Biomedical Engineering* 2002, **4**:235-260.
6. Contag CH, Contag PR: **Viewing disease progression through a bioluminescent window**. *Optics and Photonics News* 1996, **7**(1):22-23.
7. Contag CH, Ross BD: **It's not just about anatomy: In vivo bioluminescence imaging as an eyepiece into biology**. *Journal of Magnetic Resonance Imaging* 2002, **16**(4):378-387.
8. Contag CH, Spilman SD, Contag PR, Oshiro M, Eames B, Dennery P, Stevenson DK, Benaron DA: **Visualizing gene expression in living mammals using a bioluminescent reporter**. *Photochemistry and Photobiology* 1997, **66**(4):523-531.
9. Ntziachristos V, Tung CH, Bremer C, Weissleder R: **Fluorescence molecular tomography resolves protease activity in vivo**. *Nature Medicine* 2002, **8**(7):757-761.
10. Rice BW, Cable MD, Nelson MB: **In vivo imaging of light-emitting probes**. *J Biomed Opt* 2001, **6**(4):432-440.
11. Craft N, Bruhn KW, Nguyen BD, Prins R, Liau LM, Collisson EA, De A, Kolodney MS, Gambhir SS, Miller JF: **Bioluminescent imaging of melanoma in live mice**. *Journal of Investigative Dermatology* 2005, **125**(1):159-165.

12. Kuo C, Coquoz O, Troy TL, Xu H, Rice BW: **Three-Dimensional Reconstruction of In Vivo Bioluminescent Sources Based on Multi-Spectral Imaging**. *J Biomed Opt* 2007, **12**(2):024007.
13. Wang G, Cong W, Durairaj K, Qian X, Shen H, Sinn P, Hoffman E, McLennan G, Henry M: **In vivo mouse studies with bioluminescence tomography**. *Opt Express* 2006, **14**(17):7801-7809.
14. Wang G, Hoffman EA, McLennan G: **Systems and methods for bioluminescent computed tomographic reconstruction**. In.: US Patent Office; 2002.
15. Wang G, Hoffman EA, McLennan G, Bohnenkamp F, Colliso F, Cong WX, Jiang M, Kumar D, Li H, Li Y *et al*: **Development of the first bioluminescent CT scanner**. *Radiology* 2003, **229**:566.
16. Cong W, Wang G, Kumar D, Liu Y, Jiang M, Wang LV, Hoffman EA, McLennan G, McCray PB, Zabner J *et al*: **Practical reconstruction method for bioluminescence tomography**. *Opt Express* 2005, **13**(18):6756-6771.
17. Lv YJ, Tian J, Cong WX, Wang G, Luo J, Yang W, Li H: **A multilevel adaptive finite element algorithm for bioluminescence tomography**. *Opt Express* 2006, **14**(18):8211-8223.
18. Cong A, Wang G: **Multi-spectral bioluminescence tomography: Methodology and simulation**. *Int'l J of Biomed Imaging* 2006, **ID57614**:1-7.
19. Cong W, Wang G: **Bioluminescence tomography based on the phase approximation model**. *J Opt Soc Am A* 2010, **27**(2):174-179.
20. Cong A, Cong W, Lu Y, Santago P, Chatziioannou A, Wang G: **Differential evolution approach for regularized bioluminescence tomography**. *IEEE Trans Biomed Eng* 2010, **57**:2229-2238.
21. Petrovsky A, Schellenberger E, Josephson L, Weissleder R, Bogdanov A: **Near-infrared fluorescent imaging of tumor apoptosis**. *Cancer Res* 2003, **63**:1936-1942.
22. Sevick-Muraca EM, Reynolds JS, Troy TL, Lopez G, Paithankar DY: **Fluorescence lifetime spectroscopic imaging with measurements of photon**

migration. *Advances in Optical Biopsy and Optical Mammography* 1998, **838**:46-57.

23. Tsien RY: **The Green Fluorescent Protein**. *Annu Rev Biochem* 1998, **67**:509–544.
24. Tsien RY: **Building and breeding molecules to spy on cells and tumors**. *FEBS Letters* 2005, **579**(4):927-932.
25. Shcherbo D, Merzlyak EM, Chepurnykh TV, Fradkov AF, Ermakova GV, Solovieva EA, Lukyanov KA, Bogdanova EA, Zaraisky AG, Lukyanov S *et al*: **Bright far-red fluorescent protein for whole-body imaging**. *Nature Methods* 2007, **4**(9):741-746.
26. Hoffman RM: **Advantages of multi-color fluorescent proteins for whole-body and in vivo cellular imaging**. *J Biomed Opt* 2005, **10**:041202.
27. Hoffman RM: **The multiple uses of fluorescent proteins to visualize cancer in vivo**. *Nature Reviews Cancer* 2005, **5**(10):796-806.
28. Hoffman RM, Yang M: **Subcellular imaging in the live mouse**. *Nature Protocols* 2006, **1**(2):775-782.
29. Zacharakis G, Kambara H, Shih H, Ripoll J, Grimm J, Saeki Y, Weissleder R, Ntziachristos V: **Volumetric tomography of fluorescent proteins through small animals in vivo**. *P Natl Acad Sci USA* 2005, **102**(51):18252-18257.
30. Zacharakis G, Ripoll J: **Fluorescent protein tomography scanner for small animal imaging**. *Ieee T Med Imaging* 2005, **24**(7):878-885.
31. Ntziachristos V: **Fluorescence molecular imaging**. *Annual Review of Biomedical Engineering* 2006, **8**:1-33.
32. Schultz R, Ripoll J, Ntziachristos V: **Noncontact optical tomography of turbid media**. *Optics Letter* 2003, **18**(18).
33. Schultz R, Ripoll J, Ntziachristos V: **Experimental fluorescence tomography of tissues with noncontact measurements**. *Ieee T Med Imaging* 2004, **23**(4):492-500.

34. Zacharakis G, Kambara H: **Volumetric tomography of fluorescent proteins through small animals in-vivo**. *P Natl Acad Sci USA* 2005, **102**(51):18252-18257.
35. Wu J, Wang Y, Perelman L, Itzkan I, Dasari RR, Feld MS: **Time-Resolved Multichannel Imaging of Fluorescent Objects Embedded in Turbid Media**. *Opt Lett* 1995, **20**(5):489-491.
36. Hull EL, Nichols MG, Foster TH: **Localization of luminescent inhomogeneities in turbid media with spatially resolved measurements of cw diffuse luminescence emittance**. *Appl Optics* 1998, **37**(13):2755-2765.
37. Paithankar DY, Chen AU, Pogue BW, Patterson MS, SevickMuraca EM: **Imaging of fluorescent yield and lifetime from multiply scattered light reemitted from random media**. *Appl Optics* 1997, **36**(10):2260-2272.
38. Eppstein MJ, Dougherty DE, Troy TL, Sevick-Muraca EM: **Biomedical optical tomography using dynamic parameterization and Bayesian conditioning on photon migration measurements**. *Appl Optics* 1999, **38**(10):2138-2150.
39. Eppstein MJ, Hawrysz DJ, Godavarty A, Sevick-Muraca EM: **Three-dimensional, Bayesian image reconstruction from sparse and noisy data sets: Near-infrared fluorescence tomography**. *P Natl Acad Sci USA* 2002, **99**(15):9619-9624.
40. Roy R, Sevick-Muraca EM: **Truncated Newton's optimization scheme for absorption and fluorescence optical tomography: Part I theory and formulation**. *Opt Express* 1999, **4**(10):353-371.
41. Jiang HB: **Frequency-domain fluorescent diffusion tomography: a finite-element-based algorithm and simulations**. *Appl Optics* 1998, **37**(22):5337-5343.
42. Sevick-Muraca EM, Godavarty A, Eppstein MJ, Zhang CY, Theru S, Thompson AB, Gurfinkel M: **Fluorescence-enhanced optical imaging in large tissue volumes using a gain-modulated ICCD camera**. *Phys Med Biol* 2003, **48**(12):1701-1720.

43. Ntziachristos V, Weissleder R: **Experimental three-dimensional fluorescence reconstruction of diffuse media using a normalized Born approximation**. *Opt Lett* 2001, **26**(12):893-895.
44. Ntziachristos V, Schellenberger E, Ripoll J, Yessayan D, Graves E, Bogdanov A, Josephson L, Weissleder R: **Visualization of antitumor treatment by means of fluorescence molecular tomography with an annexin V-Cy5.5 conjugate**. *Proceedings of The National Academy of Sciences* 2004, **101**:12294-12299.
45. Lee JH, Joshi A, Sevick-Muraca EM: **Fully adaptive finite element based tomography using tetrahedral dual-meshing for fluorescence enhanced optical imaging in tissue**. *Opt Express* 2007, **15**(11):6955-6975.
46. Cong A, Wang G: **A finite-element-based reconstruction method for 3D fluorescence tomography**. *Opt Express* 2005, **13**:9847-9857.
47. Klose AD, Larsen EW: **Light transport in biological tissue based on the simplified spherical harmonics equations**. *Journal of Computational Physics* 2006, **220**:441-470.
48. Kim AD, Keller JB: **Light propagation in biological tissue**. *J Opt Soc Am A* 2003, **20**:92-98.
49. Ishimaru A: **Wave propagation and scattering in random media**. Oxford: Oxford Unversity Press; 1997.
50. Welch J, Gemert MJCv: **Optical and Thermal response of laser-irradiated tissue**: Plenum Press,New York; 1995.
51. Wang L-H, Jacques SL, Zheng L-Q: **MCML - Monte Carlo modeling of photon transport in multi-layered tissues**. *Computer Methods and Programs in Biomedicine* 1995, **47**:131-146
52. Klose AD, Hielscher AH: **Quasi-Newton methods in optical tomographic image reconstruction**. *Inverse Problems* 2003, **19**(12):387-409.
53. Schweiger M, Arridge SR, Hiraoka M, Delpy DT: **The Finite-Element Method for the Propagation of Light in Scattering Media - Boundary and Source Conditions**. *Med Phys* 1995, **22**(11):1779-1792.

54. Arridge S: **Optical tomography in medical imaging**. *Inverse Problems* 1999, **15**:R41-R93.

55. Panasyuk GY, Markel VA, Schotland JC: **Superresolution and corrections to the diffusion approximation in optical tomography**. *Appl Phys Lett* 2005, **87**:101111.

56. Bal G: **Inverse transport theory and applications**. *Inverse Problems* 2009, **25**:1-48.

57. Ripoll J, Nieto-Vesperinas M, Weissleder R, Ntziachristos V: **A fast analytical approximation for arbitrary geometries in diffuse optical tomography**. *Optics Letter* 2002, **27**(7):527-529.

58. Patterson MS, Pogue BW: **Mathematical-Model for Time-Resolved and Frequency-Domain Fluorescence Spectroscopy in Biological Tissue**. *Appl Optics* 1994, **33**(10):1963-1974.

59. Henyey LG, Greenstein IL: **Diffuse radiation in the galaxy**. *Asmphys J* 1941, **93**:70-83.

60. Joseph JH, Wiscombe WJ, Weinman JA: **The Delta-Eddington Approximation for Radiative Flux Transfer**. *J Atmos Sci* 1976, **33**:2452-2459.

61. Cheong W-F, Prahl SA, Welch AJ: **A review of the optical properties of biological tissues**. *IEEE J Quantum Electron* 1990, **26**:2166-2186.

62. Cong W, Shen H, Cong A, Wang Y, Wang G: **Modeling photon propagation in biological tissues using a generalized Delta-Eddington phase function**. *Physical Review E* 2007, **76(**5):051913.

63. Cong W, Shen H, Cong A, Wang G: **Integral equations of the photon fluence rate and flux based on a generalized Delta-Eddington phase function**. *J Biomed Opt* 2008, **13**:024016.

64. Cong A, Liu Y, Kumar D, Cong W, Wang G: **Geometrical Modeling Using Multiregional Marching Tetrahedra for Bioluminescence Tomography**. *Proc SPIE Medical Imaging* 2005, **5744**:756-763.

65. Gonzalez-Rodriguez P, Kim AD: **Light propagation in tissues with forward-peaked and large-angle scattering**. *Appl Optics* 2008, **47**(14):2599-2609.

66. Siegel A, Marota JJ, Boas D: **Design and evaluation of a continuous-wave diffuse optical tomography system**. *Opt Express* 1999, **4**:287-298.
67. Pogue BW, Geimer S, McBride TO, Jiang SD, Osterberg UL, Paulsen KD: **Three-dimensional simulation of near-infrared diffusion in tissue: boundary condition and geometry analysis for finite-element image reconstruction**. *Appl Optics* 2001, **40**(4):588-600.
68. Boyd S, Vandenberghe L: **Convex Optimization**: Cambridge University Press; 2004.
69. Chaudhari AJ, Darvas F, Bading JR, Moats RA, Conti PS, al e: **Hyperspectral and multispectral bioluminescence optical tomography for small animal imaging**. *Phys Med Biol* 2005, **50**:5421-5441.
70. Dehghani H, Davis SC, Jiang SD, Pogue BW, Paulsen KD, Patterson MS: **Spectrally resolved bioluminescence optical tomography**. *Opt Lett* 2006, **31**(3):365-367.
71. Zhao H, Doyle TC, Coquoz O, Kalish F, Rice BW, Contag CH: **Emission spectra of bioluminescent reporters and interaction with mammalian tissue determine the sensitivity of detection in vivo**. *J Biomed Opt* 2005, **10**(4):041210.
72. Comsa DC, Farrell TJ, Patterson MS: **Quantification of bioluminescence images of point source objects using diffusion theory models**. *Phys Med Biol* 2006, **51**(15):3733-3746.
73. Comsa DC, Farrell TJ, Patterson MS: **Bioluminescence imaging of point sources implanted in small animals post mortem: evaluation of a method for estimating source strength and depth**. *Phys Med Biol* 2007, **52**(17):5415-5428.
74. Wang G, Li Y, Jiang M: **Uniqueness theorems in bioluminescence tomography**. *Med Phys* 2004, **31**(8):2289-2299.
75. Jiang M, Wang G: **Image reconstruction for bioluminescence tomography**. In: *SPIE 5535:335-351, Society of Photo-Optical Instrumentation Engineers: 2004; Bellingham, WA, USA*; 2004.

76. Price KV, Storn RM, Lampinen JA: **Differential evolution**: Springer, Berlin Heidelberg; 2005.
77. Mantell N: **Evaluation of survival data and two new rank order statistics arising in its consideration**. *Cancer Chemother Rep* 1966, **50**:163-170.
78. Dautray R, Lions JL: **Evolution Problems II**, vol. 6. Berlin: Springer; 2000.
79. Michalewicz Z: **Genetic algorithms + data structures = evolution program**, 3rd rev. and extended ed. edn: Springer; 1999.
80. Shen H, Wang G: **A tetrahedron-based inhomogeneous Monte Carlo optical simulator**. *Phys Med Biol* 2010, **55**(4):947-962.
81. Alexandrakis G, Rannou FR, Chatziioannou AF: **Tomographic bioluminescence imaging by use of a combined optical-PET (OPET) system: a computer simulation feasibility study**. *Phys Med Biol* 2005, **50**(17):4225-4241.
82. Alexandrakis G, Rannou FR, Chatziioannou AF: **Effect of optical property estimation accuracy on tomographic bioluminescence imaging: simulation of a combined optical-PET (OPET) system**. *Phys Med Biol* 2006, **51**(8):2045-2053.
83. Cong AX, Hofmann MC, Cong W, Xu Y, Wang G: **Monte Carlo fluorescence microtomography**. *J Biomed Opt 16* 2011, **16**:070501.
84. Alerstam E, Svensson T, Andersson-Engels S: **Parallel computing with graphics processing units for high-speed Monte Carlo simulation of photon migration**. *J Biomed Opt* 2008, **13**(6):-.
85. Badal A, Badano A: **Accelerating Monte Carlo simulations of photon transport in a voxelized geometry using a massively parallel graphics processing unit**. *Med Phys* 2009, **36**(11):4878-4880.
86. Tickner J: **Monte Carlo simulation of X-ray and gamma-ray photon transport on a graphics-processing unit**. *Comput Phys Commun* 2010, **181**(11):1821-1832.
87. Price K, Storn R, Lampinen: **Differential Evolution: A Practical Approach to Global Optimization**. New York: Springer-Verlag; 2005.

88. Hong H, Yang K, Zhang Y, Engle JW, Feng LZ, Yang YA, Nayak TR, Goel S, Bean J, Theuer CP *et al*: **In Vivo Targeting and Imaging of Tumor Vasculature with Radiolabeled, Antibody-Conjugated Nanographene**. *Acs Nano* 2012, **6**(3):2361-2370.
89. Gollavelli G, Ling YC: **Multi-functional graphene as an in vitro and in vivo imaging probe**. *Biomaterials* 2012, **33**(8):2532-2545.
90. Yang K, Zhang SA, Zhang GX, Sun XM, Lee ST, Liu ZA: **Graphene in Mice: Ultrahigh In Vivo Tumor Uptake and Efficient Photothermal Therapy**. *Nano Lett* 2010, **10**(9):3318-3323.
91. Minchin RF, Martin DJ: **Minireview: Nanoparticles for Molecular Imaging-An Overview**. *Endocrinology* 2010, **151**(2):474-481.
92. Qian XM, Peng XH, Ansari DO, Yin-Goen Q, Chen GZ, Shin DM, Yang L, Young AN, Wang MD, Nie SM: **In vivo tumor targeting and spectroscopic detection with surface-enhanced Raman nanoparticle tags**. *Nature Biotechnology* 2008, **26**(1):83-90.
93. Tian Y, Cao WH, Luo XX, Fu Y: **Preparation and luminescence property of Gd2O2S : Tb X-ray nano-phosphors using the complex precipitation method**. *J Alloy Compd* 2007, **433**(1-2):313-317.
94. Carpenter CM, Sun C, Pratx G, Rao R, Xing L: **Hybrid x-ray/optical luminescence imaging: Characterization of experimental conditions**. *Med Phys* 2010, **37**(8):4011-4018.
95. Pratx G, Carpenter C, Sun C, Xing L: **X-ray luminescence computed tomography via selective excitation: a feasibility study**. *IEEE Trans Med Imag* 2010, **29**:1992-1999
96. Pratx G, Carpenter CM, Sun C, Rao RP, Xing L: **Tomographic molecular imaging of x-ray-excitable nanoparticles**. *Opt Lett* 2010, **35**(20):3345-3347.

PUBLICATIONS

[1] **A. Cong**, M. Hofmann, W. Cong, Y. Xu, and G. Wang, "Monte Carlo fluorescence microtomography," J. Biomed. Opt. 16, 070501 (2011).

[2] **A. Cong**,J. Den Buijs, and D. Dragomir-Daescu, "In situ parameter identification of optimal density–elastic modulus relationships in subject-specific finite element models of the proximal femur," Medical Engineering & Physics 33, 164-173 (2011).

[3] **A. Cong**, W. Cong, Y. Lu, P. Santago, A. Chatziioannou, and G. Wang, "Differential Evolution Approach for Regularized Bioluminescence Tomography," IEEE Trans. Biomed. Eng. 57, 2229-2238 (2010).

[4] **A. Cong**, Y. Lu, W. Cong, H. Shen, A. Chatziioannou, and G. Wang, "Optical Property Characterization Based on a Phase Function Approximation Model," IEEE International Symposium on Biomedical Imaging, 446-449 (2009).

[5] G. Wang, H. Shen, Y. Liu, **A. Cong**, W. Cong, Y. Wang, and P. Dubey, "Digital spectral separation methods and systems for bioluminescence imaging," Optical Express 16, 1719-1732 (2008).

[6] W. Cong, H. Shen, **A. Cong**, G. Wang, "Integral equations of the photon fluence rate and flux based on a generalized Delta-Eddington phase function," Journal of Biomedical Optics, 13, 024016 (2008).

[7] **A. Cong**, H. Shen, W. Cong, and G. Wang, "Improving the accuracy of the diffusion model in highly absorbing media," International Journal of Biomedical Imaging 2007, Article ID 38168, 6 pages (2007).

[8] W. Cong, **A. Cong**, H. Shen, Y. Liu, and G. Wang, "Flux vector formulation for photon propagation in the biological tissue," Optics Letters 32, 2837-2839 (2007).

[9] W. Cong, H. Shen, **A. Cong**, Y. Wang, and G. Wang, "Modeling photon propagation in biological tissues using generalized Delta-Eddington phase function," Physical Review E 76, 051913 (2007).

[10] **A. Cong**, and G. Wang, "Multi-spectral bioluminescence tomography: Methodology and simulation," International Jounral of Biomedical Imaging 2006, Article ID 57614, 7 pages (2006).

[11] **A. Cong**, Y. Liu, D. Kumar, W. Cong, and G. Wang, "Geometrical Modeling Using Multiregional Marching Tetrahedra for Bioluminescence Tomography," Proc. of SPIE Vol. 5744, 756-763 (2005).

[12] W. Cong , G. Wang, D. Kumar, Y. Liu, M. Jiang, L. Wang, E. Hoffman, G. McLennan, PB. McCray, J. Zabner, and **A. Cong**, "Practical reconstruction method for bioluminescence tomography," Optics Express 13, 6756-6771 (2005).

[13] **A. Cong**, and G. Wang, "A finite-element-based reconstruction method for 3D fluorescence tomography," Optics Express 13, 9847-9857 (2005).